

RESEARCH ARTICLE SUMMARY

IMMUNOLOGY

Nucleotide metabolic rewiring enables NLRP3 inflammasome hyperactivation in obesity

Danhui Liu, Chuanli Zhou, Xiaochen Wang, Zhou Luo, Ruiyao Xu, Shanshan Huo, Lina Guo, Xuemei Luo, Shuhan Yang, Arielle Click, Janiece Vancil, Paola Barajas, Victor Mijares, Hamid Baniyadi, Nan Yan, Jan Rehwinkel, Dustin C. Hancks, Elizabeth H. Chen, Shuang Liang, Zhenyu Zhong*



Full article and list of author affiliations: <https://doi.org/10.1126/science.adq9006>

INTRODUCTION: Obesity has emerged as a major public health crisis, particularly in developed nations, owing to its strong association with chronic diseases such as type 2 diabetes, metabolic dysfunction-associated steatotic liver disease, cardiovascular disorders, neurodegenerative diseases, and cancer. A hallmark of obesity is persistent, low-grade inflammation, which exacerbates disease progression. However, the precise molecular mechanisms linking obesity to immune dysregulation remain elusive.

RATIONALE: The Nod-like receptor pyrin domain-containing 3 (NLRP3) inflammasome, which predominantly functions in macrophages, plays a central role in regulating sterile inflammation in the context of obesity-related diseases. In response to sterile tissue injury or stress, NLRP3 activation by damage-associated molecular patterns triggers the production of pro-inflammatory cytokines, such as interleukin (IL)-1 β , which disrupts insulin signaling, fuels adipose and hepatic inflammation, and accelerates metabolic disease progression. Although it is known that oxidized mitochondrial DNA (ox-mtDNA) can activate the NLRP3 inflammasome, whether and how obesity affects macrophage mtDNA and NLRP3 inflammasome sensitivity remain poorly understood.

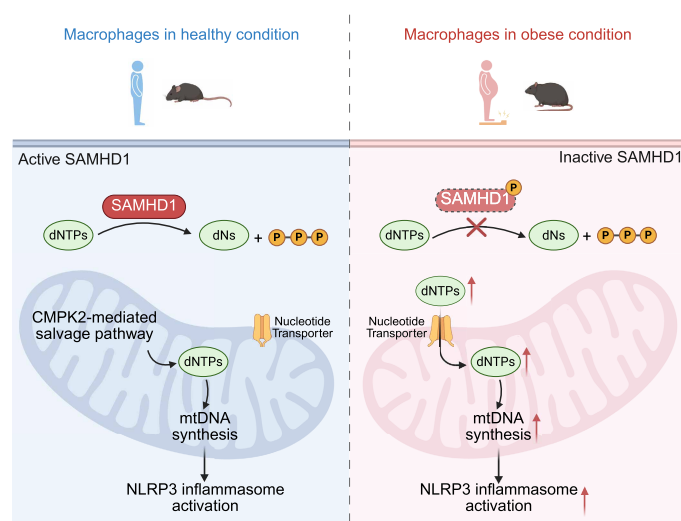
RESULTS: In comparison to cells isolated from lean individuals and mice, macrophages isolated from obese individuals and mice fed on a high fat diet had NLRP3 inflammasome hyperactivation and excessive IL-1 β production. This hyperactive phenotype correlated with an increase in mtDNA abundance in macrophages from obese individuals and mice. The obesity-induced mtDNA elevation occurred independently of the cytidine

monophosphate kinase 2 (CMPK2)-dependent mitochondrial deoxynucleoside triphosphate (dNTP) salvage pathway. Instead, obesity impaired the function of SAM and HD domain-containing protein 1 (SAMHD1), a highly conserved dNTP hydrolase, leading to aberrant cytosolic dNTP accumulation. These excess dNTPs could be transported into mitochondria through nucleotide transporters, fueling uncontrolled mtDNA synthesis, excessive ox-mtDNA production, and subsequent NLRP3 hyperactivation. Consistently, genetic ablation of SAMHD1 caused NLRP3 hyperactivation in zebrafish and mice and predisposed mice to obesity-driven metabolic disorders. Blocking dNTP transport into mitochondria abolished NLRP3 hyperactivation in macrophages from both obese individuals and SAMHD1-deficient mice.

CONCLUSION: We conclude that obesity rewires macrophage nucleotide metabolism to enable NLRP3 inflammasome hyperactivation and uncontrolled inflammation, thereby precipitating disease progression. Moreover, we also identified SAMHD1 as a macrophage-intrinsic inhibitor restraining NLRP3 inflammasome activation from fish to humans and delineated the underlying mechanism of action. Because blocking dNTP mitochondrial transport alleviated NLRP3 inflammasome hyperactivation in macrophages isolated from obese individuals and those from SAMHD1-deficient mice, our results suggested that targeting mitochondrial dNTP transport may offer a therapeutic strategy to mitigate obesity-induced inflammation and its associated diseases. □

*Corresponding author. Email: zhenyu.zhong@utsouthwestern.edu Cite this article as D. Liu et al., *Science* 391, eadq9006 (2026). DOI: 10.1126/science.adq9006

Obesity increased SAMHD1 phosphorylation and thereby compromised its deoxynucleoside triphosphatase function, ultimately leading to aberrant accumulation of cytosolic dNTPs in macrophages. These dNTPs are then transported into mitochondria through nucleotide transporters to provide excessive building blocks for new mtDNA synthesis, resulting in the bypass of CMPK2-mediated nucleotide salvage pathway, ultimately leading to uncontrolled mtDNA neosynthesis, overproduction of ox-mtDNA, and subsequent NLRP3 inflammasome hyperactivation.



IMMUNOLOGY

Nucleotide metabolic rewiring enables NLRP3 inflammasome hyperactivation in obesity

Danhui Liu¹, Chuanli Zhou¹, Xiaochen Wang^{1†}, Zhou Luo², Ruiyao Xu¹, Shanshan Huo^{1‡}, Lina Guo¹, Xuemei Luo¹, Shuhan Yang¹, Arielle Click¹, Janiece Vancil¹, Paola Barajas¹, Victor Mijares¹, Hamid Baniasadi³, Nan Yan¹, Jan Rehwinkel⁴, Dustin C. Hancks¹, Elizabeth H. Chen^{2,5,6,7}, Shuang Liang^{1,5}, Zhenyu Zhong^{1,5*}

Obesity is a major disease risk factor due to obesity-associated hyperinflammation. We found that obesity induced Nod-like receptor pyrin domain-containing 3 (NLRP3) inflammasome hyperactivation and excessive interleukin (IL)-1 β production in macrophages by disrupting SAM and HD domain-containing protein 1 (SAMHD1), a deoxynucleoside triphosphate (dNTP) hydrolase crucial for nucleotide balance. This caused aberrant accumulation of dNTPs, which can be transported into mitochondria, and initiated mitochondrial DNA (mtDNA) neosynthesis, which increased the presence of oxidized mtDNA and triggered NLRP3 hyperactivation. Deletion of SAMHD1 promoted NLRP3 hyperactivation in cells isolated from zebrafish, mice, and humans. SAMHD1-deficient mice showed elevated circulating IL-1 β , insulin resistance, and metabolic dysfunction-associated steatohepatitis. Blocking dNTP mitochondrial transport prevented NLRP3 hyperactivation in macrophages from obese patients and SAMHD1-deficient mice. Our study revealed that obesity by inhibiting SAMHD1 rewired macrophage nucleotide metabolism, thereby triggering NLRP3 inflammasome hyperactivation to drive disease progression.

Obesity has become prevalent, particularly within developed countries, and is a public health concern (1–4). Obesity promotes the development of chronic and noncommunicable diseases, including type 2 diabetes, metabolic dysfunction-associated steatotic liver disease, cardiovascular disorders, Alzheimer's disease, dementia, and cancer (1–9). A hallmark of obesity is dysregulated inflammation, characterized by persistent, low-grade production of proinflammatory cytokines, causing nonresolving inflammatory responses that in turn precipitate the pathogenic progression of obesity-associated diseases (2, 10–15). However, how obesity leads to dysregulation of inflammation has remained poorly understood.

Sterile inflammation is caused by disruption to tissue homeostasis in the absence of invading pathogens and is largely driven by activation of an innate immune sensor of tissue damage, called the Nod-like receptor pyrin domain-containing 3 (NLRP3) inflammasome (16–22). Aberrant activation of the NLRP3 inflammasome in macrophages

triggers caspase-1-dependent proteolytic processing of immature proinflammatory cytokines, namely pro-interleukin (IL)-1 β and pro-IL-18, into the mature forms which can promote inflammation (18, 19, 21, 23, 24) and is linked to obesity-associated diseases (4, 5). For example, IL-1 β can interfere with insulin signaling in pancreatic β cells, causing insulin resistance, thereby driving systemic metabolic dysregulation and development of type 2 diabetes (25, 26). In the liver, obesity-induced IL-1 β can initiate a proinflammatory cytokine signaling cascade that, ultimately, dismantles macrophage efferocytosis to establish chronic hepatic inflammation, thereby promoting the transition from benign fatty liver (simple steatosis) to metabolic dysfunction-associated steatohepatitis, cirrhosis, and even hepatocellular carcinoma (27–29).

Mitochondria contribute to the activation of the NLRP3 inflammasome (16, 25, 30–42). In addition to inducing de novo pro-IL-1 β synthesis and elevating NLRP3 expression, priming signals, such as lipopolysaccharides (LPS) and poly(I:C), also up-regulate cytidine monophosphate kinase 2 (CMPK2), a rate-limiting enzyme operating within the mitochondrial deoxynucleoside triphosphate (dNTP) salvage pathway that supplies dNTPs required for mitochondrial DNA (mtDNA) neosynthesis in macrophages (33, 37, 38). During the activation step, when macrophages are stimulated with NLRP3 activators, including adenosine triphosphate (ATP), microbial toxins, and particulate substances, mitochondria become damaged, resulting in the overproduction of mitochondrial reactive oxygen species (mtROSs) (25, 31, 33, 35, 37, 38). Relative to the existing mtDNA, the newly synthesized mtDNA, not yet fully packaged into “nucleoids” by a histone-like molecule called TFAM (transcription factor A, mitochondria), are more susceptible to mtROS-induced damage, thereby serving as the major source for oxidized mtDNA (ox-mtDNA) (33, 38). Ox-mtDNA is excised by mitochondrial FEN1 endonuclease into small fragments and subsequently released from mitochondria into the cytosol through the mitochondrial permeability transition pore (mPTP) and voltage-dependent anion channel (VDAC) and/or BAK and BAX pores (37, 43). Fragmented ox-mtDNA binds to and activates NLRP3 to induce inflammasome assembly and caspase-1-mediated maturation and secretion of IL-1 β (31, 33, 44).

In this study, we aimed to determine whether obesity disrupts the regulation of the NLRP3 inflammasome, a central mediator of inflammation in metabolic disease. We investigated the molecular mechanisms by which obesity alters inflammasome activation in macrophages with the goal of identifying therapeutic targets to mitigate obesity-associated inflammation.

Results

Obesity triggers NLRP3 inflammasome hyperactivation

To investigate the impact of obesity on NLRP3 inflammasome activation in humans, we obtained primary PBMCs from lean individuals [body mass index (BMI) \leq 25 kg/m²] and those from obese patients (BMI \geq 40 kg/m²) and isolated CD14⁺ monocytes. After differentiating these cells into monocyte-derived macrophages (MDMs), we found that, in response to NLRP3 activator stimulation, MDMs from obese individuals produced higher levels of mature IL-1 β , had increased caspase-1 activation, and elevated markers of pyroptosis compared to cells from lean subjects (Fig. 1, A to D). We did not detect differences in tumor necrosis factor (TNF) production or the expression of NLRP3 inflammasome components and pro-IL-1 β between MDMs from obese and lean individuals (Fig. 1, B and C). Bone marrow-derived macrophages (BMDMs) from C57BL/6 mice fed with a high-fat diet (HFD) also exhibited an NLRP3 inflammasome hyperactive phenotype compared to cells isolated from mice fed with a normal diet (ND) (Fig. 1, E to G).

Primary peritoneal macrophages (PMs) from HFD-fed mice also displayed NLRP3 inflammasome hyperactivation relative to cells from ND-fed mice (Fig. 1, H to J). By contrast, TNF production induced by

¹Department of Immunology, University of Texas Southwestern Medical Center, Dallas, TX, USA. ²Department of Molecular Biology, University of Texas Southwestern Medical Center, Dallas, TX, USA. ³Department of Biochemistry, University of Texas Southwestern Medical Center, Dallas, TX, USA. ⁴Medical Research Council Translational Immune Discovery Unit, Medical Research Council Weatherall Institute of Molecular Medicine, Radcliffe Department of Medicine, University of Oxford, Oxford, UK. ⁵Harold C. Simmons Comprehensive Cancer Center, University of Texas Southwestern Medical Center, Dallas, TX, USA. ⁶Department of Cell Biology, University of Texas Southwestern Medical Center, Dallas, TX, USA. ⁷Hamon Center for Regenerative Science and Medicine, University of Texas Southwestern Medical Center, Dallas, TX, USA. *Corresponding author. Email: zhenyu.zhong@utsouthwestern.edu †Present address: Center of Hepato-Pancreato-Biliary Surgery, The First Affiliated Hospital of Sun Yat-Sen University, Guangzhou, Guangdong Province, China. ‡Present address: College of Life Sciences, Hebei Agricultural University, Baoding, Hebei Province, China.

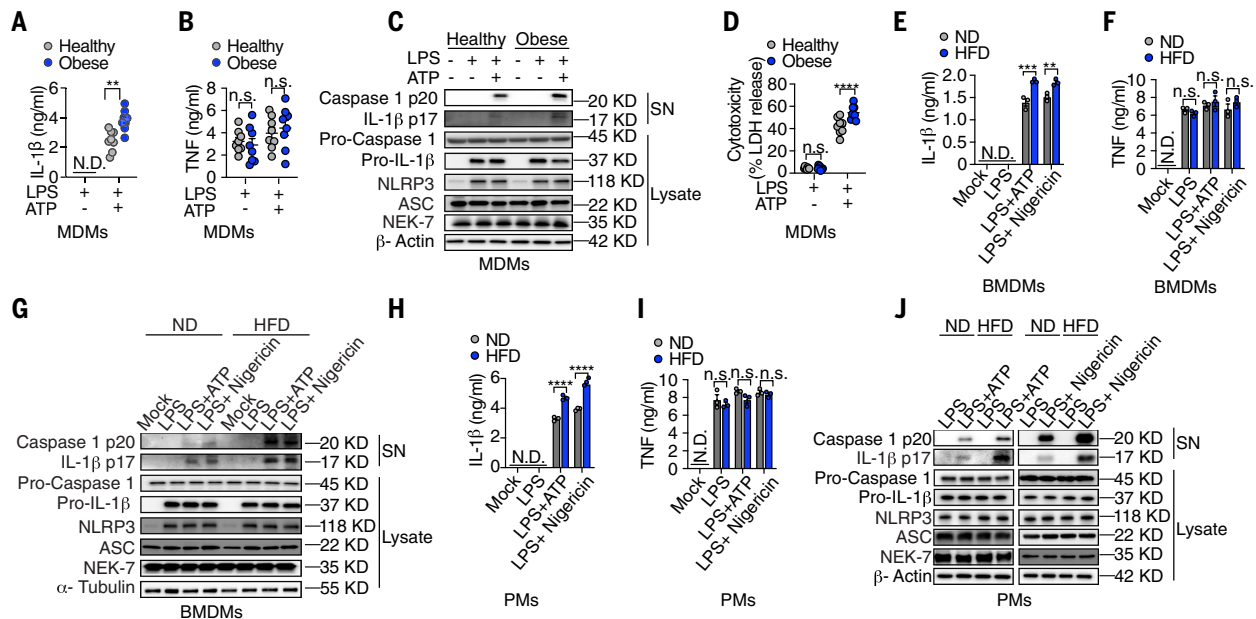


Fig. 1. Obesity triggers NLRP3 inflammasome hyperactivation in both human and mouse macrophages. (A to D) PBMC-MDMs from healthy and obese individuals were primed with LPS followed by ATP stimulation. [(A) and (B)] ELISA analysis of IL-1 β (A) and TNF (B) in cell culture supernatants. (C) Immunoblot analysis of supernatants (SN) and cell extracts (lysate) for cleaved caspase-1 (Casp1 p20) and mature IL-1 β (p17). (D) Cytotoxicity assay measured by LDH release. (E to J) C57BL/6 mice were fed with an ND or an HFD for 24 weeks. [(E) to (G)] BMDMs from ND or HFD mice were primed with LPS followed by stimulation with indicated NLRP3 activators. [(E) and (F)] ELISA analysis of IL-1 β (E) and TNF (F) in cell culture supernatants. (G) Immunoblot analysis of supernatants (SN) and cell extracts (lysate) for cleaved caspase-1 (Casp1 p20) and mature IL-1 β (p17). [(H) to (J)] Primary PMs from ND or HFD mice were primed with LPS followed by stimulation with indicated NLRP3 activators. [(H) and (I)] ELISA analysis of IL-1 β (H) and TNF (I) in cell culture supernatants. (J) Immunoblot analysis of supernatants (SN) and cell extracts (lysate) for cleaved caspase-1 (Casp1 p20) and mature IL-1 β (p17). In graphs, dots represent data for individual humans or mice, and bars represent the mean \pm SEM. $n = 3$ replicates for (E), (F), (H), and (I); $n = 8$ individuals per group for (A), (B), and (D); $n = 3$ healthy and 3 obese individuals for (C). All in vitro experiments were repeated independently at least three times. ** $P < 0.01$; *** $P < 0.001$; **** $P < 0.0001$; two-sided unpaired t test for (A); two-way ANOVA for (B), (D) to (F), (H), and (I). N.D., not detectable; n.s., not significant.

LPS in murine macrophages was unaffected by dietary obesity (Fig. 1, F and I). We concluded that obesity promoted hyperactivation of the NLRP3 inflammasome and overproduction of IL-1 β in both humans and mice.

Obesity-induced NLRP3 hyperactivation relies on mitochondrial DNA

We sought to identify the molecular mechanism underlying NLRP3 inflammasome hyperactivation in macrophages during obesity. Because mitochondrial damage and subsequent production of ox-mtDNA are pivotal events driving NLRP3 inflammasome activation (31, 33, 34, 37, 43, 44), we assessed mtDNA abundance and the extent of its oxidation. We observed an increase in the abundance of mtDNA in CD14⁺ monocytes from obese individuals compared with those from lean controls (fig. S1, A and B). This difference was further maintained in MDMs upon LPS-induced inflammasome priming (fig. S1, C and D). Consequently, the production of ox-mtDNA following stimulation with ATP was elevated in human MDMs isolated from obese individuals (fig. S1E).

The increased mtDNA abundance and ox-mtDNA production as well as hyperactivation of NLRP3 inflammasome observed in human MDMs from obese individuals were inhibited by eliminating mtDNA using ethidium bromide (EtBr) (fig. S1, F to L) or through genetic ablation of TFAM (fig. S1, M to S). Additionally, pretreatment with 8-hydroxy-2'-deoxyguanosine (8-OH-dG), a compound known to competitively inhibit the binding of ox-mtDNA to NLRP3 (31, 45), alleviated NLRP3 inflammasome hyperactivation without affecting TNF production (fig. S1, T to V) in human MDMs from obese individuals.

Thus, we concluded that mtDNA played a role in obesity-induced NLRP3 inflammasome hyperactivation and ruled out the possibility

of gain-of-function somatic mutations in genes encoding inflammasome components in mediating the hyperactive phenotype.

Mitochondrial nucleotide salvage pathway is dispensable for obesity-induced NLRP3 hyperactivation

We investigated how obesity might cause elevated mtDNA in macrophages. We assessed the expression of DNA polymerase γ (POL γ), the enzyme responsible for mtDNA replication, and found no difference in the expression of both POL γ subunits (POL-G1/G2) in human CD14⁺ monocytes between lean and obese individuals (fig. S2, A and B). Furthermore, the expression of other factors essential for mtDNA synthesis, such as mitochondrial single-stranded DNA binding protein (mtSSB), TWINKEL, and CMPK2, were also unaltered (fig. S2, A to D).

Moreover, genetic ablation of *CMPK2* using CRISPR/Cas9 in human MDMs from obese individuals had no effect on mtDNA neosynthesis or ox-mtDNA production and failed to rectify NLRP3 inflammasome hypersensitivity (fig. S2, E to K). By contrast, *CMPK2* ablation reduced mtDNA neosynthesis, ox-mtDNA production, and NLRP3 inflammasome activation in MDMs from lean individuals (fig. S2, E to K).

Thus, we concluded that *CMPK2*-dependent nucleotide analogism only contributed to NLRP3 inflammasome activation in macrophages from lean but not obese individuals. This prompted us to investigate whether obesity caused dysregulation of nucleotide catabolism.

Obesity compromises the function of SAMHD1

The primary regulator of cellular dNTP catabolism is the evolutionarily conserved dNTP hydrolase SAM and HD domain-containing protein 1 (SAMHD1) (46, 47). As a deoxyguanosine triphosphate (dGTP)-stimulated enzyme, SAMHD1 degrades all four types of dNTPs into

respective deoxynucleosides (dNs) and inorganic triphosphates, thereby governing cellular dNTP homeostasis (46, 49). We measured SAMHD1 expression in monocytes and MDMs from both lean and obese individuals but found no discernible difference (Fig. 2A-D).

For SAMHD1 to operate as a deoxynucleoside triphosphatase (dNTPase), it must form a homotetrameric complex (48), a process intricately regulated by phosphorylation (48, 50). The phosphorylation of monomeric SAMHD1 at threonine-592 (T592) in human (or T603 in mouse) inhibits its ability to form tetramers, thereby nullifying its dNTPase activity (48, 51). We observed that the levels of phosphorylated SAMHD1 (p-SAMHD1) were elevated and that the formation of SAMHD1 tetramers was decreased in monocytes from obese individuals compared with that from lean controls (Fig. 2C-G). This suggested that obesity compromised the function of SAMHD1 in human monocytes. A similar defect in SAMHD1 tetramer formation was also observed in PBMC-MDMs derived from obese but not lean individuals (Fig. 2H).

We also observed elevated p-SAMHD1 and reduced SAMHD1 tetramer formation in adipose tissue-associated macrophages (ATMs) isolated from HFD-fed wild-type (WT) C57BL/6 mice when compared with those from ND-fed control mice (Fig. 2, I to M). The level of total SAMHD1 was unchanged in ATMs isolated from mice fed different diets (Fig. 2, I, J, and N).

Thus, these findings indicated that obesity compromised the function of SAMHD1 in human and mouse myeloid cells by inducing its phosphorylation.

SAMHD1 restrains NLRP3 inflammasome hyperactivation

To explore the potential regulatory role of SAMHD1 in NLRP3 inflammasome activation, we treated BMDMs isolated from *Samhdi*^{+/+} and *Samhdi*^{-/-} mice with LPS and various NLRP3 activators in vitro. *Samhdi*^{-/-} BMDMs exhibited a two- to threefold enhancement in IL-1 β but not TNF production compared with that in *Samhdi*^{+/+} cells when stimulated with NLRP3 activators such as ATP, nigericin, dioleoyl-3-trimethylammonium propane (DOTAP) liposomes, and alum microcrystals (Fig. 2O and fig. S3A).

SAMHD1 deficiency had no impact on the expression of NLRP3 inflammasome components or pro-IL-1 β during inflammasome priming (fig. S3B). Instead, NLRP3-dependent ASC (apoptosis-associated speck-like protein containing a CARD) oligomerization and speck formation were heightened in *Samhdi*^{-/-} BMDMs after NLRP3 activator stimulation (Fig. 2, P to R). Moreover, caspase-1 activation was intensified in NLRP3 activator-treated *Samhdi*^{-/-} BMDMs, evidenced by increased Casp1 p20, elevated FLICA signals (indicative of active caspase-1), and enhanced caspase-1-dependent pyroptosis (Fig. 2, S to U). The production of ox-mtDNA and its cytosolic release were also increased in *Samhdi*^{-/-} BMDMs relative to WT control cells (Fig. 2, V and W). Noncanonical NLRP3 inflammasome activation by intracellular LPS was also enhanced when SAMHD1 was absent (fig. S3, C and D). In contrast to NLRP3, the activation of NLRC4 and AIM2 inflammasomes, achieved through flagellin and poly(dA:dT) transfection, respectively, remained unaffected by SAMHD1 deficiency (fig. S3, E and F), indicating that SAMHD1 regulated NLRP3 inflammasome activity specifically. Knockdown of SAMHD1 in human primary MDMs also led to increased ox-mtDNA production and enhanced NLRP3 inflammasome activation (Fig. 2X and fig. S3, G to J).

Consistent with their key roles in vertebrate cellular circuitry, evolutionary analysis indicated that SAMHD1, NLRP3 inflammasome components, and other nucleotide metabolic enzymes were present in the zebrafish genome (fig. S4 and data S1). Genetic deletion of SAMHD1 in zebrafish larvae using the CRISPR/Cas9 system also led to heightened NLRP3 inflammasome activation in vivo (Fig. 2, Y and Z).

Given that SAMHD1 is primarily recognized for degrading dNTPs into dNs and triphosphates (46, 50, 52), we investigated whether the dNTPase activity was essential for SAMHD1-dependent restriction of

NLRP3 inflammasome hyperactivation. We transduced *Samhdi*^{+/+} and *Samhdi*^{-/-} BMDMs with lentiviruses expressing either WT human SAMHD1 or two dNTPase-inactive SAMHD1 mutants (53) and assessed their ability to rescue the NLRP3 inflammasome hyperactive phenotype. Only WT SAMHD1 but not dNTPase-inactive mutants prevented NLRP3 inflammasome hyperactivation in *Samhdi*^{-/-} BMDMs, as evidenced by reduced ASC oligomerization and speck formation, caspase-1 activation, pyroptosis [lactate dehydrogenase (LDH) release], and IL-1 β secretion (fig. S5, A to G). TNF production was not affected by the overexpression of these SAMHD1 constructs (fig. S5H). These results indicated that the dNTPase activity was crucial for SAMHD1 to restrict NLRP3 inflammasome hyperactivation.

SAMHD1 is activated during inflammasome priming

To understand how SAMHD1 was regulated during inflammasome priming and activation, we assessed its expression and phosphorylation status. Despite its high abundance in resting BMDMs, LPS priming further elevated the expression of SAMHD1 (fig. S6, A and B). We also found that LPS priming reduced the amount of phosphorylated SAMHD1 (p-SAMHD1), which was detected by an antibody specifically recognizing T603 of mouse SAMHD1 (equivalent to T592 in human SAMHD1) (fig. S6, A and B). This correlated with an enhanced tetramer formation detected by an antibody recognizing the total SAMHD1 (fig. S6, A and B). These results suggested that SAMHD1 was activated during inflammasome priming.

The phosphorylation status of SAMHD1 is regulated during the cell cycle to ensure that high levels of dNTPs are readily available before DNA synthesis (54–56) through the activity of cyclin-dependent kinases (CDKs), with CDK2 phosphorylating and inactivating SAMHD1. The endogenous inhibitor of CDK2, p21(cyclin-dependent kinase inhibitor 1A), inhibits SAMHD1 phosphorylation, consequently promoting its dNTPase activity (57). Additionally, protein phosphatase 2A (PP2A) dephosphorylates SAMHD1 to activate its dNTPase activity (58). Using the p-SAMHD1 specific antibody, we found that the decrease of p-SAMHD1 levels that we observed during inflammasome priming was blocked in cells where either p21 or PP2A were inhibited by genetic or chemical approaches (fig. S6, C to G). Thus, we concluded that SAMHD1 was up-regulated and activated during inflammasome priming and that this required both p21 and PP2A.

We reconstituted *Samhdi*^{+/+} and *Samhdi*^{-/-} BMDMs with either WT or mutant forms of human SAMHD1, where threonine at position 592 was replaced by either aspartate or valine (T592D and T592V, respectively). The phospho-mimetic T592D destabilizes SAMHD1 tetramerization by introducing the negatively charged aspartate (59), whereas the phospho-null aliphatic T592V stabilizes SAMHD1 tetramerization (59–61). In *Samhdi*^{-/-} BMDMs that expressed T592V SAMHD1, p-SAMHD1 was not detected, consistent with the epitope for the antibody being mutated, and increased formation of SAMHD1 tetramers was detected with attenuated inflammasome activation (fig. S6, H to J). In *Samhdi*^{-/-} BMDM cells that expressed the phospho-mimetic T592D SAMHD1, the formation of the SAMHD1 tetramer was decreased, and it did not decrease the inflammasome hyperactivation phenotype (fig. S6, H to J). We concluded that SAMHD1-mediated inflammasome phenotypes were dependent on its phosphorylation status.

SAMHD1 restrains NLRP3 hyperactivation by limiting mtDNA neosynthesis and ox-mtDNA production

Our data suggested that the dNTPase activity of SAMHD1 prevented NLRP3 inflammasome hyperactivation; we therefore asked whether this occurred through regulating mtDNA. We treated BMDMs with low-dose EtBr to deplete mtDNA (figs. S7 and S8, A and B) and found that it attenuated IL-1 β release, caspase-1 activation, and pyroptosis in *Samhdi*^{-/-} BMDMs without perturbation of TNF production (fig. S8, C to G). We also observed an elevated level of mtDNA in *samhdi*^{-/-} zebrafish,

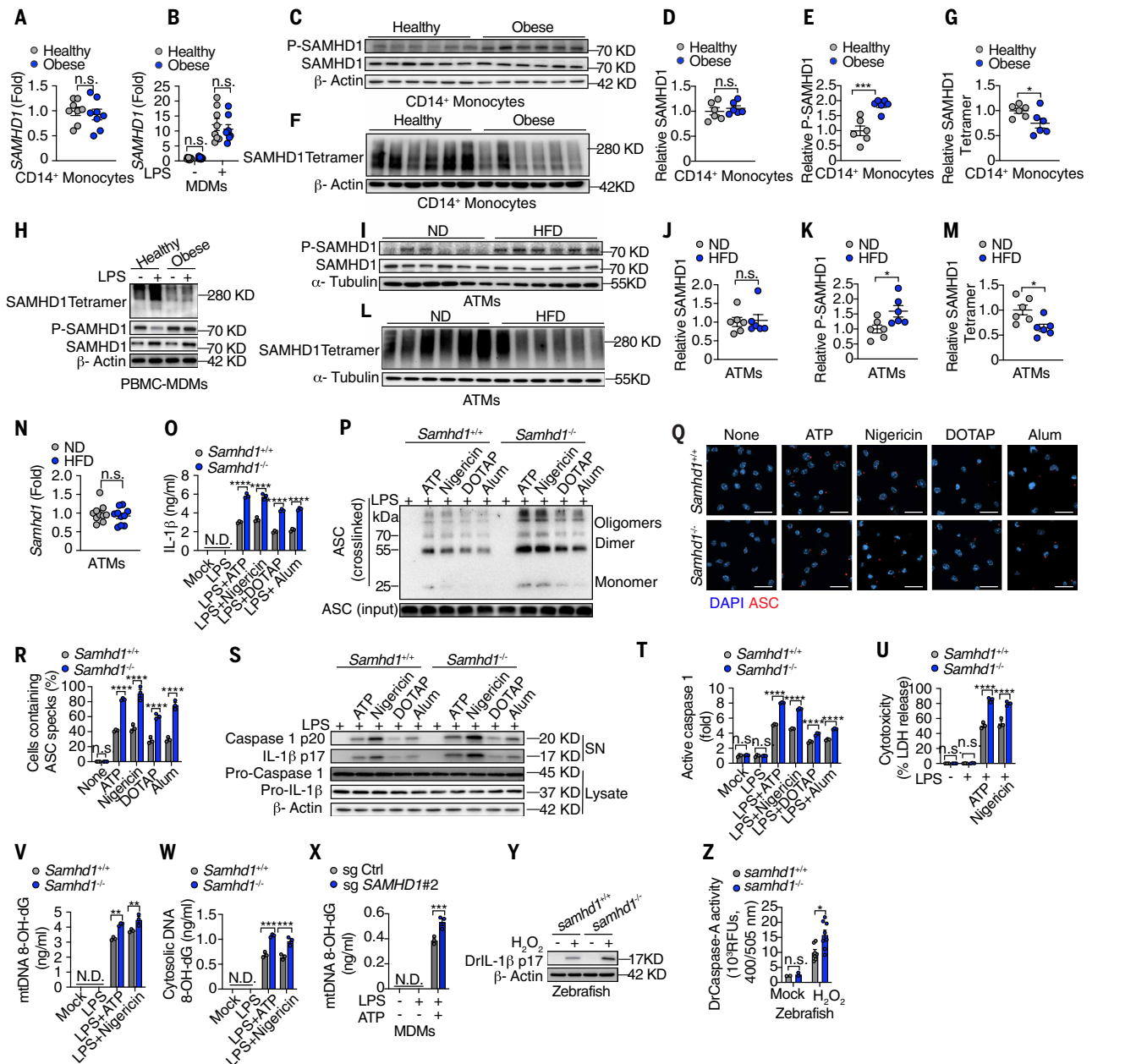


Fig. 2. SAMHD1, whose function is compromised by obesity, restrains NLRP3 inflammasome hyperactivation from fish to human. (A and B) Reverse transcription (RT)-qPCR analysis of *SAMHD1* mRNA in CD14⁺ monocytes from PBMCs (A) and PBMC-MDMs (B) of healthy and obese individuals with or without LPS priming. (C) Immunoblot analysis of phosphorylated and total SAMHD1 in CD14⁺ monocytes from PBMCs of healthy and obese individuals. (D and E) Densitometry analysis of (C). (F) Immunoblot analysis of tetramerized SAMHD1 in CD14⁺ monocytes from PBMCs of healthy and obese individuals. (G) Densitometry analysis of (F). (H) Immunoblot analysis of phosphorylated, total, and tetramerized SAMHD1 in PBMC-MDMs of healthy and obese individuals before and after LPS priming. (I) Immunoblot analysis of phosphorylated and total SAMHD1 in primary ATMs isolated from epididymal adipose tissue from ND- or HFD-fed mice. (J and K) Densitometry analysis of (I). (L) Immunoblot analysis of tetramerized SAMHD1 in primary ATMs isolated from epididymal adipose tissue from mice fed with ND or HFD. (M) Densitometry analysis of (L). (N) RT-qPCR analysis of *Samhd1* mRNA in primary ATMs isolated from epididymal adipose tissue from mice fed with ND or HFD. (O to W) *Samhd1*^{+/+} and *Samhd1*^{-/-} BMDMs were primed with LPS (200 ng/ml) for 4 hours, followed by stimulation with different NLRP3 inflammasome activators [ATP (4 mM) or nigericin (10 μM) for 45 min; DOTAP liposomes (100 μg/ml) or alum (500 μg/ml) for 4 hours]. (O) ELISA analysis of supernatant IL-1β. (P) Immunoblot analysis of ASC oligomerization in cross-linked cytosolic pellets. [(Q) and (R)] Representative immunofluorescence images (Q) and quantification (R) of ASC speck formation. Scale bars, 20 μm. *n* = 3 different microscopic fields per group; original magnification, × 60. (S) Immunoblot analysis of supernatants (SN) and cell extracts (lysate) for cleaved caspase-1 (Casp1 p20) and mature IL-1β (p17). (T) Relative caspase 1 activation as measured by the FLICA probe. (U) Cytotoxicity analysis measured by LDH release. (V and W) Amounts of mtDNA 8-OH-dG within mitochondria (V) or in the cytosol (W). (X) Amounts of mtDNA 8-OH-dG in healthy and obese PBMC-MDMs transduced with sgRNAs targeting *SAMHD1* or control sgRNA (sg Ctrl) followed by LPS + ATP stimulation. (Y and Z) Seventy-two hours postfertilization (hpf), *samhd1*^{+/+} and *samhd1*^{-/-} larvae were immersed in 10 mM H₂O₂ for 40 min. (Y) Immunoblot analysis of zebrafish larvae lysate for cleaved DrIL-1β. (Z) Fluorogenic substrate detection of DrCaspase-A activation. In graphs, dots show data for individual humans or mice, bars show mean ± SEM [*n* = 8 individuals per group for (A) and (B); *n* = 6 individuals per group for (C) to (G); *n* = 3 healthy and 3 obese individuals for (H); *n* = 6 mice per group for (I) to (M); *n* = 10 mice per group for (N); *n* = 3 replicates for (O) and (T) to (X); *n* = 5: 23:5:16 zebrafish larvae in (Y); *n* = 2:2:7:8 zebrafish larvae in (Z)]. All in vitro experiments were repeated independently at least three times. **P* < 0.05; ***P* < 0.01; ****P* < 0.001; *****P* < 0.0001; two-sided unpaired *t* test for (A), (D) to (G), and (J) to (N). Two-way ANOVA for (B), (O), (R), (T) to (W), (X), and (Z).

and EtBr pretreatment eliminated the NLRP3 inflammasome hyperactivation phenotype (fig. S8, H to K).

In addition, we generated *Tfam*^{ΔMye} mice (*Lyz2-cre; Tfam*^{F/F}) in which TFAM was specifically deleted in myeloid cells, leading to a reduction in mtDNA (Fig. 3, A and B). We knocked down *Samhd1* in both *Tfam*^{F/F} and *Tfam*^{ΔMye} BMDMs and found that the NLRP3 inflammasome hyperactive phenotype was alleviated in SAMHD1 and TFAM-double-deficient cells (Fig. 3, C to G). By contrast, deletion of *Tfam* had no impact on TNF production (Fig. 3H).

Building upon our earlier finding that inflammasome priming triggers mtDNA synthesis (33), we investigated whether SAMHD1 regulated mtDNA neosynthesis. Compared with their WT counterparts, *Samhd1*^{-/-} BMDMs had a slight elevation of mtDNA abundance at resting state, which increased further after LPS stimulation (fig. S9, A and B). We confirmed that mtDNA abundance was elevated in *Samhd1*^{-/-} BMDMs by performing cellular fractionation and observed an increase of mtDNA only in the mitochondrial, but not the cytosolic, fraction (fig. S9, C to E). *Samhd1*^{-/-} BMDMs incorporated more EdU into mtDNA compared with *Samhd1*^{+/+} cells after LPS priming

(fig. S9F), confirming heightened mtDNA neosynthesis in the absence of SAMHD1. This correlated with increased cytosolic release of newly synthesized mtDNA upon NLRP3 activator stimulation (fig. S9F).

We extracted mitochondrial and cytosolic DNA from *Samhd1*^{+/+} and *Samhd1*^{-/-} BMDMs, which had been primed with LPS with or without a following challenge with ATP, and separated it by gel electrophoresis. LPS increased the abundance of full-length mtDNA in WT macrophages during inflammasome priming, which was then partially degraded after ATP challenge, evidenced by the appearance of 500- to ~650-bp DNA fragments in both mitochondria and cytosol (fig. S9G). This might have been due to DNA damage caused by mtROS (37). Relative to WT control cells, *Samhd1*^{-/-} BMDMs had more full-length mtDNA after LPS priming (fig. S9G). Additionally, the heightened mtDNA neosynthesis in *Samhd1*^{-/-} BMDMs positively correlated with increased mtDNA fragmentation detected in the cytosolic and mitochondrial fractions after ATP stimulation (fig. S9G).

To test whether SAMHD1 prevented NLRP3 hyperactivation through restricting mtDNA neosynthesis, we inhibited the synthesis of new mtDNA specifically in both *Samhd1*^{+/+} and *Samhd1*^{-/-} BMDMs

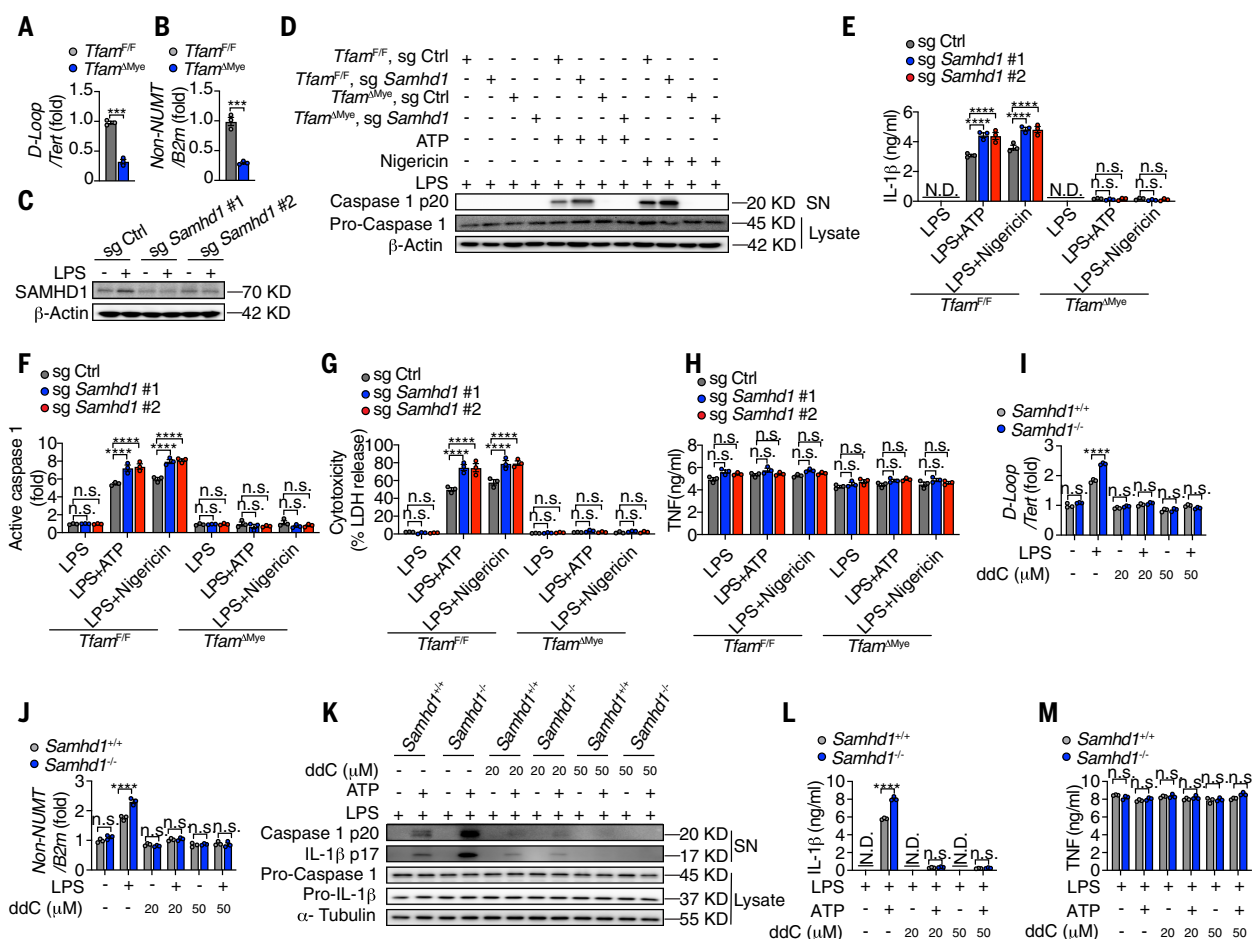


Fig. 3. SAMHD1 restrains NLRP3 inflammasome hyperactivation by limiting mtDNA neosynthesis. (A and B) qPCR analysis of relative total mtDNA amounts in *Tfam*^{F/F} and *Tfam*^{ΔMye} BMDMs. (C) Immunoblot analysis of SAMHD1 levels for knockdown efficiency validation in WT BMDMs. (D to H) *Tfam*^{F/F} and *Tfam*^{ΔMye} BMDMs were transduced with *Samhd1* sgRNA (sg *Samhd1* #1 and sg *Samhd1* #2) or control sgRNA (sg Ctrl) for 4 constitutive days starting from the 4th day of differentiation. Cells were then primed with LPS (200 ng/ml) for 4 hours, followed by stimulation with ATP or Nigericin, as indicated. (D) Immunoblot analysis of supernatants (SN) and cell extracts (Lysate) for cleaved caspase-1 (Casp1 p20) and pro-Casp1. [(E) and (H)] ELISA analysis of supernatant IL-1β (E) and TNF (H). (F) Quantification of relative caspase-1 activation by FLICA probe. (G) Cytotoxicity analysis measured by LDH release. [(I) and (J)] *Samhd1*^{+/+} and *Samhd1*^{-/-} BMDMs were pretreated with 20 or 50 μM ddC, as indicated, overnight, followed by LPS priming and ATP stimulation, as described above. [(I) and (J)] qPCR analysis of relative total mtDNA amounts in indicated groups before or after LPS priming. (K) Immunoblot analysis of supernatants (SN) and cell extracts (Lysate) for cleaved caspase-1 (Casp1 p20) and mature IL-1β (p17). [(L) and (M)] ELISA analysis of supernatant IL-1β (L) and TNF (M). In graphs, dots represent data for technical replicates, and bars represent mean ± SEM [*n* = 3 replicates for (A) and (B), (E) to (J), and (L) and (M)]. All *in vitro* experiments were repeated independently at least three times. ****P* < 0.001; *****P* < 0.0001; two-sided unpaired *t* test for (A) and (B); two-way ANOVA for (E) to (J), (L) and (M).

through a brief treatment of 2',3'-dideoxycytidine (ddC), a chain terminator for new mtDNA replication (62, 63). We found that ddC treatment, without affecting the existing mtDNA, abolished LPS-induced mtDNA neosynthesis and thereby prevented NLRP3 inflammasome hyperactivation in *Samhd1*^{-/-} BMDMs (Fig. 3, I to M, and fig. S9H). These results suggested that SAMHD1 limited mtDNA neosynthesis during inflammasome priming.

Because newly synthesized mtDNA is the major source of ox-mtDNA (33, 37) and because we observed an increase in mitochondria and its cytosolic ox-mtDNA in *Samhd1*^{-/-} BMDMs relative to their WT counterparts upon NLRP3 activator stimulation (Fig. 2, V and W), we reasoned that inhibiting mtDNA oxidation and its cytosolic localization should prevent NLRP3 inflammasome hypersensitivity in *Samhd1*^{-/-} BMDMs.

Samhd1^{-/-} BMDMs produced more mtROS than their WT counterparts upon NLRP3 activator stimulation (fig. S10A). Overexpression of WT SAMHD1 reduced mtROS production in BMDMs stimulated with NLRP3 activators (fig. S10B). Pretreatment with a mitochondria-specific ROS scavenger, Mito-TEMPO, attenuated NLRP3 inflammasome activation in *Samhd1*^{-/-} BMDMs compared with that in vehicle-treated controls without affecting TNF production (fig. S10, C to E). Likewise, pretreatment of *Samhd1*^{-/-} BMDMs with 8-OH-dG, which is known to competitively inhibit ox-mtDNA binding to NLRP3 (37), alleviated NLRP3 inflammasome hyperactivation without affecting TNF production in a dose-dependent manner (fig. S10, F to L). By contrast, pretreatment with dG, the nonoxidized counterpart of 8-OH-dG, failed to prevent inflammasome hyperactivation (fig. S10, F to L). Moreover, blocking the mPTP and VDACS prevented cytosolic release of ox-mtDNA and rescued NLRP3 inflammasome hyperactivation in *Samhd1*^{-/-} BMDMs without affecting TNF (fig. S10, M to P). Based on these results, we concluded that SAMHD1 prevented NLRP3 inflammasome hyperactivation by restricting mtDNA neosynthesis, decreasing the production of ox-mtDNA, and limiting assembly of the NLRP3 inflammasome.

Cytosolic dNTP influx to mitochondria drives NLRP3 inflammasome hyperactivation

Macrophages are terminally differentiated, postmitotic cells wherein cellular dNTPs are partitioned by the mitochondrial double membrane into two discrete compartments: the cytosolic and mitochondrial dNTP pools (16). SAMHD1, serving as the dominant dNTP hydrolase, contributes to sustaining a low level of dNTPs in the cytosol by degrading all four species of deoxyribonucleotides (46, 47, 49). We found that, relative to those in *Samhd1*^{+/+} BMDMs, the levels of all four species of dNTPs were elevated in *Samhd1*^{-/-} BMDMs before and after inflammasome priming (Fig. 4, A to H, and fig. S12, A and B).

WT macrophages rely exclusively on the nucleotide salvage synthesis pathway operating within mitochondria for dNTP supply (16, 33). CMPK2 is essential for mtDNA neosynthesis in WT macrophages during inflammasome priming (33). *Samhd1*^{-/-} BMDMs exhibited comparable CMPK2 expression levels to *Samhd1*^{+/+} cells before and after inflammasome priming (fig. S11A). In line with previous reports (33, 38), knocking down *Cmpk2* in *Samhd1*^{+/+} BMDMs resulted in reduced caspase-1 maturation, IL-1 β secretion, and pyroptotic cell death without affecting TNF (fig. S11, B to F). By contrast, silencing *Cmpk2* in *Samhd1*^{-/-} BMDMs failed to regulate these corresponding indexes (fig. S11, B to F).

We generated *Samhd1* and *Cmpk2*-double-knockout mice and compared NLRP3 inflammasome activities in BMDMs from WT, single-, and double-knockout littermate mice. In BMDMs with functional SAMHD1, depletion of CMPK2 decreased inflammasome activation (fig. S11, G to J). However, in the absence of SAMHD1, CMPK2 deficiency did not impair NLRP3 inflammasome activation (fig. S11, G to J).

Given that SAMHD1 deficiency resulted in aberrant buildup of dNTPs (Fig. 4, A to H, and fig. S12, A and B), we hypothesized that the

accumulated dNTPs could be transported from cytosol into mitochondria through mitochondrial nucleotide transporters. This might fuel mtDNA neosynthesis, potentially bypassing the CMPK2-mediated mitochondrial dNTP salvage pathway. We knocked down the mitochondrial nucleotide transporters, pyrimidine nucleotide carrier 1/2 (PNC1/2), in BMDMs (fig. S13A). Although neither mitochondrial nor cytosolic dNTP pools were affected in *Samhd1*^{+/+} BMDMs with or without nucleotide transporter silencing, we observed a reduction of all four dNTPs within mitochondria of *Samhd1*^{-/-} BMDMs with PNC1/2 deficiency (Fig. 4, I to L). The lower mitochondrial dNTP pool in *Samhd1*^{-/-} BMDMs after PNC1/2 silencing correlated with the NLRP3 inflammasome being less hyperactivated (Fig. 4, M to O). Furthermore, upon blocking cytosolic dNTP transport to mitochondria, mtDNA neosynthesis in *Samhd1*^{-/-} BMDMs was similar to that in *Samhd1*^{+/+} BMDMs (fig. S13, B to F). We concluded that inhibiting the import of cytosolic dNTPs to mitochondria prevented NLRP3 inflammasome hyperactivation in *Samhd1*^{-/-} BMDMs. Moreover, the dNTPs transported from cytosol to mitochondria in *Samhd1*^{-/-} BMDMs supported mtDNA neosynthesis without a contribution from the CMPK2-mediated salvage pathway.

We found that supplementing cell culture medium of WT murine BMDMs with excessive dNs (200 or 400 μ M), which are salvaged into dNTPs after cellular uptake (64), increased mtDNA neosynthesis during inflammasome priming, elevated caspase-1 activation, and augmented IL-1 β production upon ATP stimulation without affecting pro-IL-1 β or TNF levels (Fig. 4, P to T). Furthermore, we observed that supplementing cells with dNs eradicated the differences in mtDNA neosynthesis and NLRP3 inflammasome activation between WT and SAMHD1-deficient macrophages (Fig. 4, P to T). These findings supported the notion that SAMHD1 restricted NLRP3 inflammasome activation by limiting cellular dNTP accumulation.

SAMHD1 prevents NLRP3-dependent immunopathology in vivo

To assess the in vivo role of SAMHD1 in restraining NLRP3 inflammasome activation, we subjected *Samhd1*^{+/+} and *Samhd1*^{-/-} mice to three NLRP3-driven acute inflammation models: (i) LPS-induced sepsis, (ii) alum-induced peritonitis, and (iii) D-galactosamine (GalN)- and LPS-induced fulminant hepatitis (34, 65–67). In the sepsis model, *Samhd1*^{-/-} mice exhibited elevated serum IL-1 β (but not TNF) and increased mortality following intraperitoneal LPS injection (fig. S14, A to C). This phenotype was reversed by pretreatment of an NLRP3-specific inhibitor MCC950 (fig. S14A). In the alum-induced peritonitis model, *Samhd1*^{-/-} mice showed heightened peritoneal IL-1 β and increased neutrophil or monocyte infiltration (fig. S14, D to G). By contrast, peritonitis induced by zymosan, a toll-like receptor 2 agonist (68), resulted in similar immune cell recruitment across genotypes (fig. S14, H and I), excluding a general immune cell migratory defect. In the GalN/LPS model, *Samhd1*^{-/-} mice displayed increased serum alanine aminotransferase (ALT), severe liver damage, and enhanced caspase-1 activation in hepatic macrophages (fig. S14, J to L). We concluded that SAMHD1 limited NLRP3 inflammasome activation and protected against inflammation-induced pathology in vivo.

SAMHD1 protects mice from obesity-induced metabolic disorders

To investigate the role of macrophage SAMHD1 in obesity, we generated myeloid-specific SAMHD1-deficient mice (*Samhd1* ^{Δ Mye}) by crossing *Samhd1*^{F/F} mice, which carry loxP-flanked alleles of *Samhd1* gene, with *Ly2-Cre* mice. We subjected *Samhd1*^{F/F} and *Samhd1* ^{Δ Mye} mice to HFD for 24 weeks. Despite similar body weight and composition (fig. S15), *Samhd1* ^{Δ Mye} mice developed insulin resistance and glucose intolerance (Fig. 5, A and B). They also showed elevated serum IL-1 β , an indicator of NLRP3 inflammasome activation during obesity (26, 69), without changes in TNF (Fig. 5, C and D). ATMs from HFD-fed *Samhd1* ^{Δ Mye} mice had elevated levels of dNTPs and mtDNA (Fig. 5, E to J, and fig. S12, C and D), accompanied by enhanced oxidative

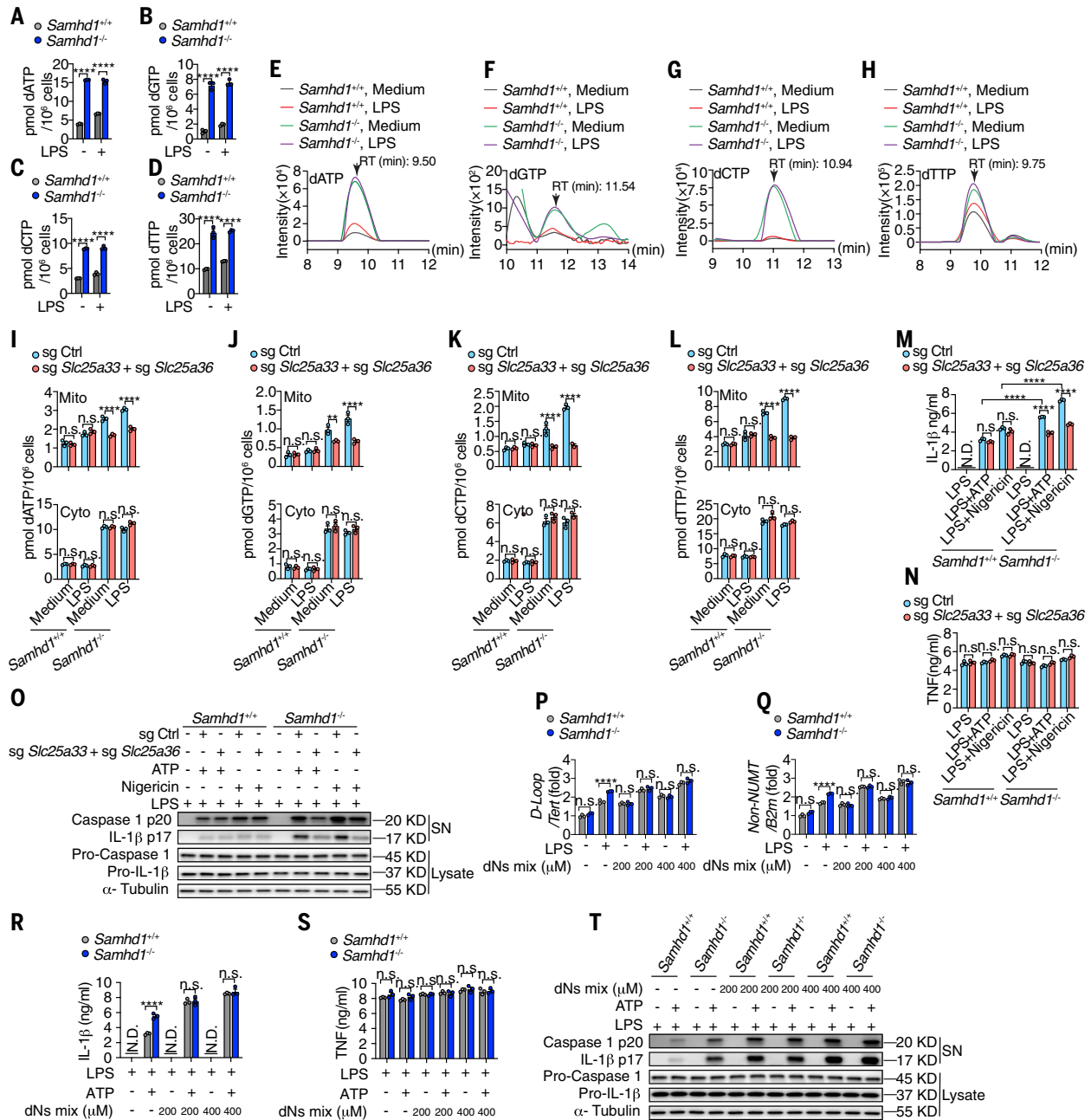


Fig. 4. The influx of cytosolic dNTPs into mitochondria drives NLRP3 inflammasome hyperactivation in SAMHD1-deficient macrophages. (A to D) qPCR quantification of cellular dNTPs in *Samhd1*^{+/+} and *Samhd1*^{-/-} BMDMs before and after LPS priming. (E to H) Representative HPLC chromatograms of cellular dNTPs in *Samhd1*^{+/+} and *Samhd1*^{-/-} BMDMs before and after LPS priming. Retention time (RT): dATP, 9.50 min; dGTP, 11.54 min; deoxycytidine triphosphate (dCTP), 10.94 min; deoxythymidine triphosphate (dTTP), 9.75 min. (I to O) *Samhd1*^{+/+} and *Samhd1*^{-/-} BMDMs were transduced with sgRNAs targeting *Slc25a33*, *Slc25a36*, or control sgRNA (sg Ctrl) for 4 constitutive days starting from the 4th day of differentiation. Cells were then primed with LPS (200 ng/ml) for 4 hours, followed by stimulation with ATP or Nigericin, as indicated. [(I) to (L)] qPCR quantification of mitochondrial (top) and cytosolic (bottom) dNTPs in indicated groups before and after LPS priming. [(M) and (N)] ELISA analysis of supernatant IL-1β (M) and TNF (N). (O) Immunoblot analysis of supernatants (SN) and cell extracts (Lysate) for cleaved caspase-1 (Casp1 p20) and mature IL-1β (p17). (P to T) *Samhd1*^{+/+} and *Samhd1*^{-/-} BMDMs were incubated with a mixture of all four deoxyribonucleosides (dNs mixed at 200 and 400 μM for each nucleoside separately) for 7 days during differentiation. Cells were then plated and primed with LPS (200 ng/ml) for 4 hours, followed by stimulation with ATP. [(P) and (Q)] qPCR analysis of relative total mtDNA amounts in indicated group before and after LPS priming. [(R) and (S)] ELISA analysis of supernatant IL-1β (R) and TNF (S). (T) Immunoblot analysis of supernatants (SN) and cell extracts (Lysate) for cleaved caspase-1 (Casp1 p20) and mature IL-1β (p17). In graphs, dots represent data for technical replicates, and bars represent mean ± SEM [n = 3 replicates for (A) to (H), (I) to (N), and (P) to (S)]. Cells were pooled from three mice per group for (E) to (H). All in vitro experiments were repeated independently at least three times. **P < 0.01; ****P < 0.0001; two-way ANOVA.

phosphorylation (fig. S16, A and B), but mitochondrial mass was unchanged (fig. S16, C to G).

Samhd1^{ΔMyc} mice lack SAMHD1 in both macrophages and neutrophils. However, SAMHD1 deficiency did not affect the ability of neutrophils to produce IL-1 β or TNF nor change their mtDNA abundance (fig. S17, A to D). Despite SAMHD1's known role in suppressing virus-induced type I interferons (IFNs) (47), we did not detect circulating type I IFNs in *Samhd1*^{F/F} and *Samhd1*^{ΔMyc} mice before or after HFD feeding (fig. S17E). Moreover, type I IFN genes (e.g., *Ifn α 4*/*Ifn β*) or IFN-stimulated genes (ISGs) were unchanged in adipose and liver tissues after 24 weeks of HFD feeding (fig. S17, F and G). Thus, we concluded that type I IFN signaling did not contribute to the metabolic phenotype in *Samhd1*^{ΔMyc} mice.

Consistent with elevated IL-1 β , *Samhd1*^{ΔMyc} mice showed increased hepatic active caspase-1 (Fig. 5, K and L) and reduced phosphorylated AKT (p-AKT) compared with that of controls (Fig. 5, M and N), indicating impaired insulin signaling. These mice also exhibited higher liver triglycerides (Fig. 5O), elevated serum ALT or AST levels (Fig. 5, P and Q), increased hepatic inflammation, and greater fibrosis after 24 weeks of HFD (Fig. 5R–U).

Global SAMHD1 deficiency (*Samhd1*^{−/−}) in mice largely recapitulated the metabolic phenotypes of *Samhd1*^{ΔMyc} mice, except for unchanged liver steatosis (fig. S18). By contrast, *Cmpk2*^{−/−} mice showed no differences in metabolic or inflammatory responses to HFD compared with in WT littermates (fig. S19), suggesting that obesity-driven nucleotide metabolism rewiring bypasses CMPK2. CMPK2 deficiency

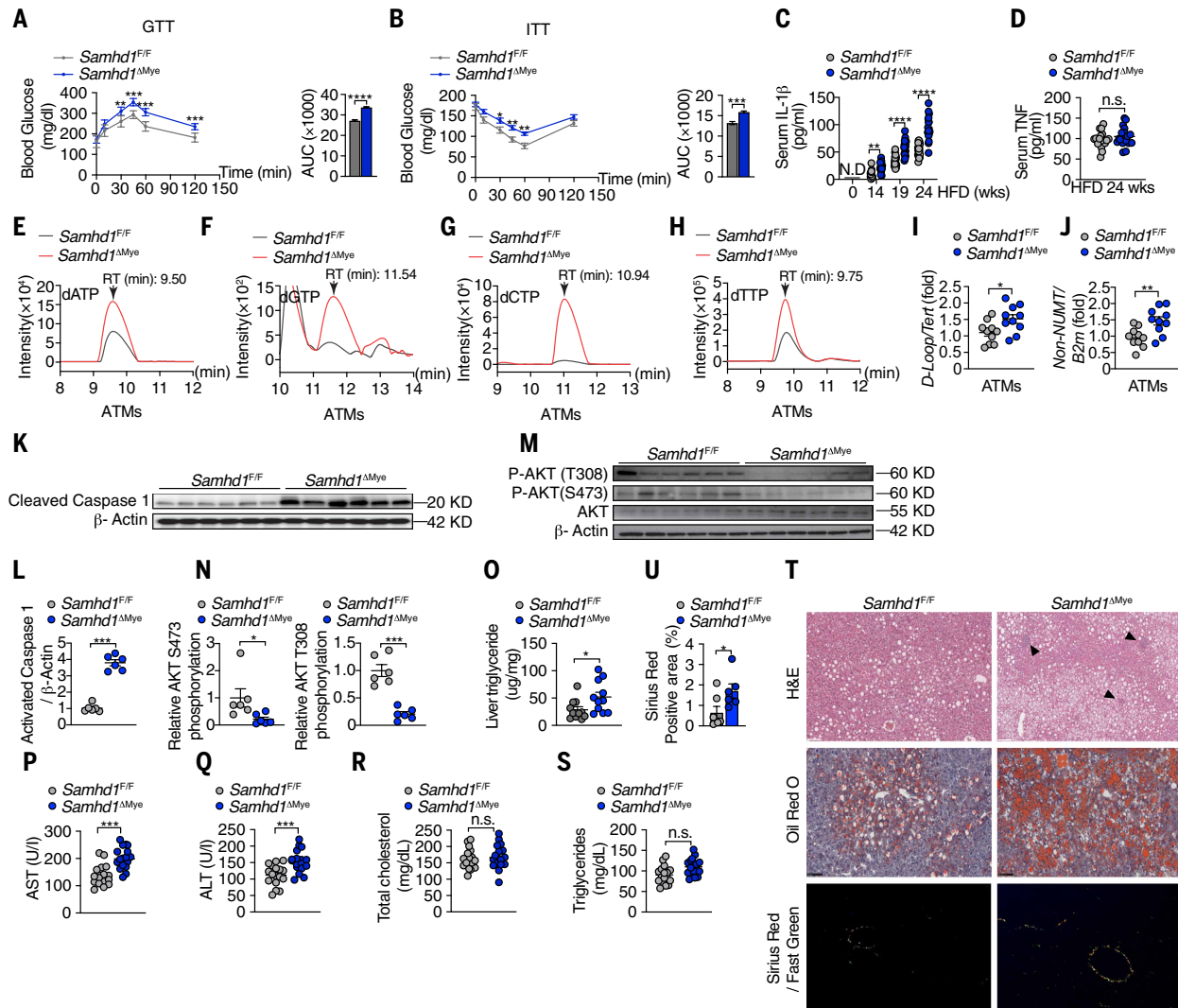


Fig. 5. SAMHD1 protects mice against obesity-induced metabolic syndromes. Six-week-old *Samhd1*^{F/F} and *Samhd1*^{ΔMyc} mice were fed with an HFD for 24 weeks. (A) Glucose tolerance test (GTT) results (left) and the area under the curve (AUC) (right). (B) Insulin tolerance test (ITT) results (left) and the AUC (right). (C and D) ELISA analysis of serum IL-1 β (C) and TNF (D) levels at indicated time points after HFD feeding. (E to H) Representative HPLC chromatograms of cellular dNTPs in primary ATMs. Retention time (RT): dATP, 9.50 min; dGTP, 11.54 min; dCTP, 10.94 min; dTTP, 9.75 min. (I and J) qPCR analysis of relative total mtDNA amounts. (K) Immunoblot analysis of epididymal white adipose tissue (eWAT) extracts for active caspase-1. (L) Densitometry analysis of (K). (M) Immunoblot analysis of liver tissue extracts for phosphorylated and total AKT levels. (N) Densitometry analysis of (M). (O) Amounts of liver triglyceride per mg of tissue. (P to S) Serum AST (P), ALT (Q), total cholesterol (R), and triglyceride (S) levels. (T) Representative histological results of liver sections stained with H&E, Oil-red-O, and Sirius red/fast green. Sirius red/fast green staining was detected under polarized light. Arrow heads indicate immune cell infiltration. Scale bars, 100 μ m; three to five different microscopic fields per sample. (U) Quantification of Sirius red-positive area in (T). In graphs, dots represent data for individual mice, and bars represent mean \pm SEM [$n = 17$ mice per group for (A) to (D) and (P) to (S); $n = 6$ mice per group for (K) to (N); $n = 11$ mice per group for (O); $n = 6$ to 7 mice per group for (U); $n = 10$ mice per group for (I) and (J); cells were pooled from 8 to 10 mice per group for (E) to (H)]. * $P < 0.05$; ** $P < 0.01$; *** $P < 0.001$; **** $P < 0.0001$; two-sided unpaired t test for (A), (B), (D), (I), (J), (L), (N) to (S), and (U); two-way ANOVA for (C).

conferred protection against alum-induced peritonitis (fig. S20), which indicated that CMPK2 may regulate NLRP3 inflammasome activation in nonobese contexts.

Blocking dNTP influx to mitochondria alleviates obesity-induced NLRP3 hyperactivation

Based on our findings, we hypothesized that blocking mitochondrial dNTP import could reverse the elevated activation of the NLRP3 inflammasome associated with SAMHD1 deficiency in human immune cells. Indeed, relative to those from lean individuals, monocytes from obese individuals had elevated dNTP levels (Fig. 6, A to L, and fig. S12, E and F), and CRISPR-mediated deletion of *PNC1/2* reduced mtDNA neosynthesis, caspase-1 activation, IL-1 β production, and pyroptosis without affecting TNF (Fig. 6, M to S). We concluded that obesity-induced NLRP3 hyperactivation stemmed from dysfunctional SAMHD1

and could be mitigated by targeting mitochondrial dNTP transport (fig. S21).

Discussion

Dysregulated inflammation contributes to obesity-associated diseases (1, 3–5, 10), yet its underlying causes remain poorly understood. We found that obesity impaired the function of SAMHD1, an evolutionarily conserved dNTPase, thereby rewiring macrophage nucleotide metabolism to drive NLRP3 inflammasome hyperactivation and pathological inflammation, fueling disease progression in the context of hypernutrition.

Eukaryotic cells maintain separate dNTP pools in the cytoplasm and mitochondria, divided by the impermeable inner mitochondrial membrane (16). In healthy macrophages, the mitochondrial dNTP supply depends on the CMPK2-mediated salvage pathway (33), as

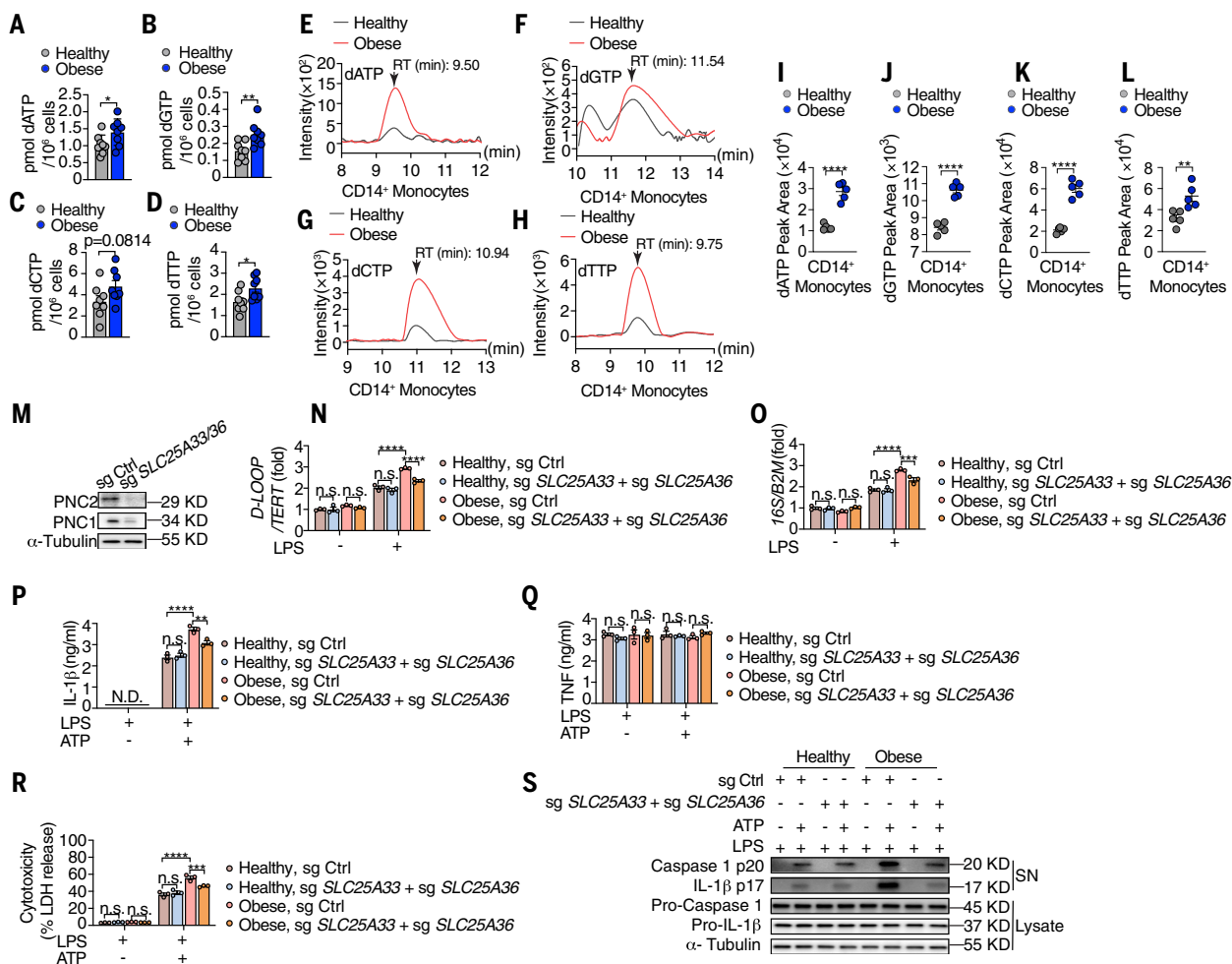


Fig. 6. Blocking dNTP influx to mitochondria eliminates obesity-induced NLRP3 hyperactivation. (A to D) qPCR quantification of cellular dNTPs in CD14⁺ monocytes from PBMCs from healthy and obese individuals. (E to H) Representative HPLC chromatograms of cellular dNTPs in CD14⁺ monocytes from PBMCs from healthy and obese individuals. Retention time (RT): dATP, 9.50 min; dGTP, 11.54 min; dCTP, 10.94 min; dTTP, 9.75 min. (I to L) HPLC chromatograms peak area in CD14⁺ monocytes from PBMCs from healthy and obese individuals. (M) Immunoblot analysis of PNC1 and PNC2 levels for knockdown efficiency validation in healthy PBMC-MDMs. (N to S) PBMC-MDMs from healthy and obese individuals were transduced with sgRNAs targeting *SLC25A33* and *SLC25A36* or control sgRNA (sg Ctrl) for 4 constitutive days starting from the 4th day of differentiation. Cells were then primed with LPS (200 ng/ml) for 4 hours, followed by ATP stimulation. [(N) and (O)] qPCR analysis of relative total mtDNA amounts of indicated PBMC-MDMs before and after LPS priming. [(P) and (Q)] ELISA analysis of supernatant IL-1 β (P) and TNF (Q). (R) Cytotoxicity analysis measured by LDH release. (S) Immunoblot analysis of supernatants (SN) and cell extracts (Lysate) for cleaved caspase-1 (Casp1 p20) and mature IL-1 β (p17). In graphs, dots represent data for individual human, and bars represent mean \pm SEM. $n = 8$ individuals per group for (A) to (D); cells were pooled from three to five individuals per group for (E) to (H); and for (I) to (L), each dot represents one HPLC sample pooled from three to five individuals per group. $n = 3$ technical replicates for (N) to (R). All in vitro experiments were repeated independently at least three times. * $P < 0.05$; ** $P < 0.01$; *** $P < 0.001$; **** $P < 0.0001$; two-sided unpaired t test for (A) to (D) and (I) to (L); two-way ANOVA for (N) to (R).

SAMHD1 keeps cytosolic dNTPs low through its dNTPase activity (46, 47). CMPK2 is essential for NLRP3 activation in healthy cells. In this work, we found that obesity impaired SAMHD1 by promoting its phosphorylation, which disrupted tetramerization and enzymatic activity, leading to cytosolic dNTP accumulation. These dNTPs could be transported into mitochondria, bypassing the CMPK2 pathway (33, 70), driving excessive mtDNA neosynthesis, ox-mtDNA overproduction, and NLRP3 inflammasome hyperactivation.

One potential advantage of rewiring nucleotide metabolism in macrophages is that it could enhance phagocytic activity during obesity. As obesity progresses, blood monocytes infiltrate adipose tissue and the liver, differentiating into macrophages that clear lipids and apoptotic cells through phagocytosis (27, 71–74). Given the high energy demands of phagocytosis and lysosomal degradation, we speculate that impaired SAMHD1 function associated with obesity may enable macrophages to support rapid mtDNA synthesis, which is critical for ATP production, as mtDNA encodes 13 essential subunits of the electron transport chain (16, 36, 75). Compared with the slow, energy-intensive CMPK2-dependent mitochondrial dNTP salvage synthesis pathway (16, 33), cytoplasmic dNTP import may offer a more efficient means for macrophages to meet the rising metabolic demands during obesity. However, this potential benefit must be balanced against the risk of NLRP3 inflammasome hyperactivation, which can drive inflammation, tissue damage, insulin resistance, and metabolic dysfunction.

We found that blocking cytoplasmic dNTP import into mitochondria through PNC1/2 inhibition reversed NLRP3 inflammasome hyperactivation in macrophages from obese and SAMHD1-deficient mice. It should be noted that PNC1/2 are not pan-dNTP transporters, as they do not transport dATP. The mitochondrial dATP decrease after their depletion likely reflects disrupted nucleotide balance rather than direct transport. This may arise from (i) reduced dATP demand owing to stalled mtDNA replication; (ii) salvage pathway alterations from pyrimidine deficiency; (iii) stress-induced expansion of transporter specificity, permitting limited dATP import; or (iv) PNC1/2 depletion, which may indirectly disrupt mitochondrial enzymes regulating dATP synthesis or turnover.

Supporting the central role of nucleotide metabolism in innate immunity, a previous report demonstrated that nucleotide pool imbalance activates mtDNA-dependent cGAS-STING signaling (76). Loss-of-function mutations in SAMHD1 leads to Aicardi-Goutières syndrome (AGS) in humans, a severe early-onset neuroinflammatory disorder (46, 47, 77). Notably, all known AGS-associated genes encode nucleotide metabolic enzymes (78), suggesting a fundamental link between nucleotide turnover and immune activation. It is thus important to explore whether other AGS-related genes also regulate NLRP3 inflammasome activity and whether its dysregulation contributes to AGS pathogenesis.

Beyond its role in restricting NLRP3 inflammasome activation, SAMHD1 also inhibits the RIG-I/MDA5/MAVS pathway through distinct mechanisms (79, 80). SAMHD1 is inhibited or degraded in myeloid cells during infection by retroviruses and herpesviruses (47, 52, 81–83). Therefore, it is possible that down-regulation of SAMHD1 may act to enhance NLRP3 and/or RIG-I/MDA5/MAVS activity in infected cells, which could have an impact during viral-bacterial coinfections.

Materials and methods

Human tissues

Human PBMC samples (1×10^8 cells per sample) from 28 healthy donors (BMI ≤ 25 kg/m²) and 28 donors with obesity (BMI ≥ 40 kg/m²) were obtained from Charles River Laboratories. All specimens are collected under protocols with appropriate ethical approvals and informed consent from donors. The specimens provided to our lab were de-identified, and no direct interaction with human subjects occurred. All groups were comparable age- and sex-wise, and the detailed information of the patients involved in this study is listed in data S2.

Animals

LysM-Cre, and *Tfam*^{F/F} mice were purchased from Jackson Laboratories. *Samhd1*^{-/-} and *Samhd1*^{F/F} mice were described before (82, 83). *Cmpk2*^{F/F} mice, which were originally from MRC Harwell Institute (C57BL/6N-Cmpk2tm1c(KOMP)Wtsi/H mice) (38), were crossed with *E2a-Cre* (Jackson Laboratories) to generate *Cmpk2*^{-/-} mice. To obtain myeloid cell specific genetic deletions, *LysM-Cre* mice were crossed with *Tfam*^{F/F} mice and *Samhd1*^{F/F} mice to generate *Tfam*^{ΔMye} and *Samhd1*^{ΔMye} mice, respectively. *Samhd1*^{-/-} and *Cmpk2*^{-/-} mice were used to generate *Samhd1* and *Cmpk2* double-knocked out mice. Euthanasia was performed by either CO₂ or isoflurane anesthesia. All mice used in this study were in a C57BL/6 background and were bred and maintained at the University of Texas Southwestern Medical Center (UTSW) and were treated in accordance with guidelines of the Institutional Animal Care and Use Committee. All animal studies were approved by the Institutional Animal Care and Use Committee (IACUC) at UTSW.

Reagents

Ultrapure LPS (*Escherichia coli* O111:B4), ATP, monosodium urate crystal (MSU), Nigericin, Flagellin, Poly (dA:dT), and MCC950 were from Invivogen. DOTAP liposomes were made by Encapsula NanoSciences. Pan caspase inhibitor Z-VAD-FMK (FMK001) was from R&D Systems. 2',3'-Dideoxycytidine (ddC, D5782-100MG) was from Sigma. 2'-Deoxyadenosine monohydrate (D8668), 2'-Deoxyguanosine monohydrate (D0901), 2'-Deoxycytidine hydrochloride (D0776), and Thymidine (T1895) were from Sigma. PP2A inhibitor Okadaic Acid (HY-N6785) was from MedChemExpress. 8-Hydroxy-2'-deoxyguanosine (8-OH-dG, 89320) and its non-oxidized form 2'-deoxyguanosine (dG, 9002864) were from Cayman Chemical. Ethidium Bromide solution (E1385), Mito-TEMPO (SML0737), LPS (L2630, for in vivo injection), and D-Galactosamine (G1639) were from Sigma. Imject Alum (77161) was from Thermo Scientific. Click-iT EDU microplate kit was from Life Technologies. OxiSelect Oxidative DNA damage enzyme-linked immunosorbent assay (ELISA) kit (8-OHdG quantitation kit, STA-320) was from Cell Biolabs. L929 cells (from ATCC) were authenticated before delivery to our laboratory and were routinely tested negative for mycoplasma contamination. Antibodies used for immunoblot analysis were: anti-mouse caspase-1 (AG-20B-0042-C100, Adipogen), anti-human caspase-1 (AG-20B-0048-C100, Adipogen), anti-mouse IL-1 β (12426S, Cell Signaling Technologies), anti-human IL-1 β (12703S, Cell Signaling Technologies), anti-zebrafish IL-1 β (16806-1-AP, ProteinTech), anti-NLRP3 (AG-20B-0014-C100, Adipogen), anti-ASC (AG-25b-0006-C100, Adipogen), anti-NEK7 (ab133514, Abcam), anti-SAMHD1 (Gift kindly provided by Dr. Jan Rehwinkel), anti-SAMHD1 (12586-1-AP, ProteinTech), anti-Phospho-SAMHD1 (89930S, Cell Signaling Technologies), anti-Phospho-AKT T308 (9275, Cell Signaling Technologies), anti-Phospho-AKT S473 (9271, Cell Signaling Technologies), anti-AKT (9272, Cell Signaling Technologies), anti-PNC1 (ab97820, Abcam), anti-PNC2 (GTX119934, GeneTex), anti-CMPK2 (NBPI-80653, Novus Biologicals), anti-mouse TFAM (ARP36993, Avivabio), anti-human TFAM (8076S, Cell Signaling Technologies), anti-PP2A-B55 (4593S, Cell Signaling Technologies), anti-p21 Waf1/Cip1 (E2R7A) (37543, Cell Signaling Technologies), anti-COX IV (4850, Cell Signaling Technologies), anti-Cytochrome c (4280, Cell Signaling Technologies), anti-Histone H3 (17168-1-AP, Protein Tech), anti-mtSSB (12212-1-AP, Protein Tech), anti-POLG1 (ab154310, Abcam), anti-POLG2 (A6695, ABclonal), anti-TWINKLE (13435-1-AP, Protein Tech), anti-TOM20 (sc17764, Santa Cruz), anti-rabbit IgG, HRP linked Antibody (7074S, Cell Signaling Technologies), anti-mouse IgG, HRP linked Antibody (7076S, Cell Signaling Technologies), anti- β -actin (B8434, Sigma-Aldrich), and anti- α -tubulin (T5168, Sigma-Aldrich). Antibodies used for immunofluorescence and flow cytometry were from eBioscience and Biolegend: Donkey anti-Rabbit IgG (H+L) Highly Cross-Absorbed Secondary Antibody, Alexa Fluor 488 (A21207, Invitrogen), Donkey

anti-Goat IgG (H+L) Highly Cross-Absorbed Secondary Antibody, Alexa Fluor Plus 594; CD45 (m30-F11-V500), CD11b (mM1/70-eF450/eF660), F4/80 (mBM8-PE/ FITC), Ly-6G (1A8-Ly6g/ PerCP-eFluor 710), CD16/CD32 Monoclonal Antibody (KT1632), and Ly6C (mHK1.4-eF450).

Cell isolation, culture, and stimulation

Femurs and tibias from indicated 8- to 12-week-old male mice were used to generate bone-marrow-derived macrophages (BMDMs). Bone marrow cells were cultured in high glucose DMEM supplemented with 10% FBS, 20% L929-cell conditioned medium, and 100 U/mL penicillin-streptomycin for 7 days at 37°C with 5% CO₂. Mouse peritoneal macrophages were collected from peritoneal cavity 4 days after intraperitoneal injection of thioglycolate (Millipore). Mouse adipose tissue macrophages (ATMs) were sorted using anti-mouse F4/80 microbeads (130-110-443, Miltenyi Biotec) from the stromal vascular fraction (SVF) pellets isolated from mouse epididymal white adipose tissue (eWAT) as described (84, 85). Mouse neutrophils were obtained using Mouse Neutrophil Isolation Kit (130-097-658, Miltenyi Biotec) according to manufacturer's instructions. Human CD14⁺ monocytes were positively selected from PBMCs using anti-human CD14 microbeads (130-050-201, Miltenyi Biotec). Human monocyte-derived macrophages (PBMC-MDMs) were generated by culturing PBMCs (combined from at least 3 healthy and 3 obese individuals unless otherwise noted) in the presence of human M-CSF (50 ng/mL, 216-MC, R&D Systems) for 7 days. For Figs. 1, A, B, and D, and 2B, as well as figs. S1, C and D, and S2C, PBMC-MDMs from each individual were cultured and differentiated separately, and each dot in the figure indicates sample from one individual. For stimulation, 2 × 10⁶ cells were plated in 6-well plates overnight in FBS-free DMEM medium. The following morning, after priming with ultrapure LPS (200 ng/ml) for 4 hours, cells were then stimulated with ATP (4 mM) or nigericin (100 μM) for 45 min unless otherwise indicated or DOTAP liposomes (100 μg/ml), alum (500 μg/ml) for 4 hours. For AIM2 inflammasome activation, BMDMs were primed with LPS as above, followed by transfection of poly (dA: dT) (1 μg/ml) using Lipofectamine 3000 (Life Technologies) according to manufacturer's instructions. For NLRP4 inflammasome activation, flagellin (500 ng/ml) was transfected into cells using Lipofectamine 3000, followed by incubation for 6 hours. Noncanonical NLRP3 activation was initiated by transfecting LPS (1 μg/ml) into cells using Lipofectamine 3000, followed by incubation for 6 hours. Inhibitors were added 1 hour prior to the inflammasome activators unless otherwise noted. Culture supernatants and cell lysates were collected for ELISA, immunoblot, and mtDNA analyses.

Gene knockout, silencing, and overexpression

CRISPR/Cas9-mediated endogenous gene ablation and shRNA mediated gene knock down were performed in primary mouse BMDMs and primary human PBMC-MDMs by lentiviral transduction as described previously (27, 33). LentiCRISPRV2 plasmids were used for CRISPR/Cas9-mediated gene ablation. Lentiviruses carrying the single guide RNA (sgRNA) and Cas9 were generated in HEK293T with the packaging plasmid psPAX2 and the envelope plasmid pVSV-G. Target guide sequences were as follows: sgTFAM#1: TGCCTCATCCACCGGACGA #2: CGGGTCACTGCCTCATCCAC; sgCMPK2#1: GAGGCACCACCGCCGCACTT, #2: GCTGTGCGTGCCCGTGACCC; sgSLC25A33#1: AGTCTTCAAGATTAGCTCTC, #2: TTCAGAACCTGAAAGAGTCC; sgSLC25A36#1: AGACACTACTCGTTGACAC, #2: TCAACCGAGTAGTGTCTCC; sgSAMHD1#1: CGGAAGGGGTGTTTGTAGGGG, #2: CTTAGTTATATCCAGCGAT; sgSamhd1#1: GGCTGCGAAGTTAAGTACCG, #2: CTTGGGCTGCCATCGCAGCG; sgSlc25a33#1: ACGCTGCTTCATCTCTTCGC, #2: TCGGACGGTGTATTACCCTC; sgSlc2536#1: AACGTGAGGCCCA-GTCGTGC, #2: ACGACCGCCGCGCAGCAGAA; Sigma MISSION® Lentiviral shRNA were used to knock down *Cmpk2* (TRCN0000025132, TRCN0000025131), *Ppp2r2a* (TRCN0000081365, TRCN0000012626)

and *Cdkn1a* (TRCN0000042587, TRCN0000054901). Wild-type human SAMHD1, SAMHD1 R366H, SAMHD1 R366C, SAMHD1 T592V, and SAMHD1 T592D were cloned to the retroviral vector pMXs-Puro (Cell Biolabs, RTV-012) using a NEBuilder HiFi DNA assembly cloning kit (NEB, E2621L). Retroviruses were packaged in HEK293T cells with the packaging plasmid pGag-Pol and the envelope plasmid pVSV-G. For the infection of BMDMs, freshly isolated mouse bone-marrow cells were seeded in 6-well plates (2 × 10⁵ cells/well) on day 0, followed by lentiviral infection on day 4, day 5, and day 6. Infected BMDMs were then collected at day 8 for further experiments.

RNA isolation and quantitative PCR

RNA was isolated from BMDMs and reverse transcribed into cDNA, and quantitative polymerase chain reaction (qPCR) was performed as previously described (33). Primer sequences are as follows. *Tnf* F: GACGTGGAACTGGCAGAAGAG; *Tnf* R: TTGGTGGTTTGTGAGTGTGAG; *Il6* F:GGCAATTATCTCGT GGCTTC; *Il6* R: GTAGCTATGGCGTAGGTGGC; *IL-1β* F: GCAACTGTTCTGAACTCAACT; *IL-1β* R: ATCTTTTGGGGTCCGTCACCT; *Timp1* F: GCAACTCGGACCTGTGTCATAA; *Timp1* R: CGGCCCGTGATGAGAAACT; *Acta2* F: GTCCAGACATCAGGGAGTAA; *Acta2* R: TCGGATACTTCAGCGTCAGGA; *Col1a1* F: GCTCCTCTTAGGGGCCACT; *Col1a1* R: CCACGTCTCACCAT-TGGGG; *Lipa* F: GCTCCTCTTAGGGGCCACT; *Lipa* R: CCACGTCTCACCAT-TGGGG; *Ppara* F: AGAGCCCCACTGTCTCTCTC; *Ppara* R: ACTGGTAGTCTGCAAAACCAAA; *Hprt1* F:TCAGTCAACGGGGGACATAAA; *Hprt1* R: GGGGCTGTACTGCTTAACCAG; *Samhd1* F: TGCCCGT-ATCTGTGAAGTGGAG; *Samhd1* R:GCAGTTGCGAGTGTGGAACATG; *SAMHD1* F: CTGGAACCTCCATCCCGACTAC; *SAMHD1* R: AGTAATGCCTGTGATTTCAT; *CMPK2* F:GTACCTCCTTTATTCCTGAAGCC; *CMPK2* R: ATGGCAACAACCTGGAACCTT; *Ifna4* F: CTTTCTCATGATCCTGGTAATGAT; *Ifna4* R: AATCCAAAATCCTTCTCTGCTCTC; *Ifnb* F: CAGCTCCAAGAAAGGACGAAC; *Ifnb* R: GGCAGTGTA-ACTTCTTGCAT; *Isg15* F:CTAGAGCTAGAGCCTGCAG; *Isg15* R: AGTTAGTACGGACACCAG; *Ifi44* F: CTGATTACAAAAGAAGACA-TGACAGAC; *Ifi44* R: AGGCAAAACCAAGACTCCA; *Ifit1* F:CAAGG-CAGGTTTCTGAGGAG; *Ifit1* R: GACCTGGTACCATCAGCAT; *Ifit3* F:TTCCAGCAGCACAGAAAC; *Ifit3* R: AAATTCCAGGTGAAATGGCA.

ELISA

Paired (capture and detection) antibodies and standard recombinant mouse IL-1β (from R&D Systems) and TNF (from eBioscience) were used to determine cytokine concentrations in cell culture supernatants and mouse serum as previously described (33). Human IL-1 beta/IL-1F2 DuoSet ELISA kit (DY201-05, R&D Systems) and mouse IFN-β DuoSet ELISA kit (DY8234-05, R&D Systems) were used to determine IL-1β and IFN-β concentrations respectively, according to manufacturer's instructions.

Measurement of total mtDNA

Total DNA was isolated using Allprep DNA/RNA Mini Kit (80204, QIAGEN) according to manufacturer's instructions. mtDNA was quantified by qPCR using primers specific for the mitochondrial D-loop region, 16S RNA, or a specific region of mtDNA that is not inserted into nuclear DNA (non-NUMT). Nuclear DNA encoding *Tert* and *B2m* was used for normalization. Primer sequences are as follows: mmu *D-loop* F: AATCTACCATCCTCCGTGAAACC; mmu *D-loop* R: TCAGT-TTAGCTACCCCCAAGTTTAA; mmu *Tert* F: CTAGCTCATGTGT-CAAGACCCTCTT; mmu *Tert* R: GCCAGCACGTTTCTCTCGTT; mmu *B2m* F: ATGGGAAGCCGAACATACTG; mmu *B2m* R: CAGTCTCA-GTGGGGGTGAAT; mmu *non-NUMT* F: CTAGAAACCCCGAAACCAAA; mmu *non-NUMT* R: CCAGCTATACCAAGCTCGT; hsa *D-LOOP* F: CTATCACCCCTATTAACCACTCA; hsa *D-LOOP* R: TTCGCCTGTA-ATATGACCTGA; hsa *16S* F: GCCTTCCCCCGTAAATGATA; hsa *16S* R: TTATGCGATTACCAGGCTCT; hsa *TERT* F:CTTGGAACCAAGG-ACAAAGG; hsa *TERT* R: TAAAATTATCCACATGGCTCACGT. Standard

curves of the above indicated gene used for mtDNA quantification were shown in Data S4.

Cellular fractionation and quantification of mitochondrial and cytosolic mtDNA

BMDMs were stimulated as indicated and divided into two equal aliquots. One aliquot was subjected to DNA extraction using QIAamp DNA Mini Kit (250) (51306, QIAGEN) serving as normalization controls for total mtDNA. Cytosolic and mitochondrial fractions of BMDMs were obtained from the second aliquots using a Mitochondria and Cytosol fractionation Kit for cultured cells (89874, Thermo Fisher Scientific). Mitochondrial pellets were lysed and extracted to obtain mitochondrial DNA using QIAamp DNA Mini Kit (250) (51306, QIAGEN). Supernatants were extracted to obtain cytosolic DNA using QIAquick Nucleotide Removal Columns (QIAGEN). qPCR was performed on whole cell extracts as well as mitochondrial and cytosolic fractions, and *Tert/B2m* levels from whole cell DNA served as normalization controls. For the measurement of ox-mtDNA, purified mtDNA was extracted from the cytosolic or mitochondrial fractions as indicated. The 8-OH-dG content was then quantified using OxiSelect Oxidative DNA damage ELISA kit (Cell Biolabs), per manufacturer's instructions.

Agarose gel electrophoresis of mitochondrial DNA

DNA fragmentation in mitochondria was determined as previously described (37). BMDMs were stimulated as indicated and fractionated as described above, and mitochondrial DNA was purified using AllPrep DNA/RNA Mini Kit according to manufacturer's instructions and analyzed on 1% agarose gels stained with ethidium bromide.

ASC oligomerization assay

Purification and detection of ASC aggregates was performed according to previously published protocols (86). Briefly, BMDMs (5×10^6 cells per group) were stimulated as indicated. Cells were then rinsed in ice-cold phosphate-buffered saline (PBS), scraped, and lysed in 400 μ L ice-cold lysis buffer (50 mM Tris-HCl pH 7.6, 150 mM NaCl, 1% NP-40, 1 mM EDTA, 10% glycerol, and a protease inhibitor cocktail (Invitrogen)), followed by 10 times shearing through a 21-gauge needle to completely disrupt cell membranes. Cell debris was removed by centrifuging at 250 g for 5 min at 4°C, and the supernatants were subject to centrifugation at 5,000 g for 10 min at 4°C to pellet ASC aggregates. After washing with 500 μ L PBS, the pellets were resuspended with 300 μ L lysis buffer containing 6 μ L freshly prepared Disuccinimidyl suberate (DSS, 100 mM). After DSS cross-linking at room temperature for 30 min, the reaction was terminated by adding 6 μ L 1M Tris-HCl for 15 min at room temperature followed by centrifugation at 10,000 g for 5 min at 4°C to pellet the cross-linked ASC. The pellets were resuspended in 50 μ L 2 \times protein loading buffer, boiled for 5 min at 99°C and subjected to immunoblot analysis.

SAMHD1 tetramerization detection

SAMHD1 tetramer detection was performed according to a previously reported study with slight modifications (87). In brief, cells were incubated in the presence of 0.25% (v/v) formaldehyde (FA) in culture medium at 37°C for 10 min. Cross-linking was terminated by the addition of glycine to a final concentration of 0.125 M. Cells were then washed with cold PBS and lysed with ice-cold NP-40 buffer (50 mM Tris-HCl pH 7.6, 150 mM NaCl, 1% NP-40, 1 mM EDTA, 10% glycerol) containing protease inhibitors (Invitrogen) for 10 min on ice followed by addition of protein loading buffer and immunoblot analysis.

Immunoblot analysis

Cells were lysed in RIPA buffer (25 mM Tris-HCl pH 7.6, 150 mM NaCl, 1% NP-40, 1% sodium deoxycholate, 0.1% SDS) containing a protease inhibitor cocktail (Roche, I1836153001) and a phosphatase inhibitor

cocktail (Sigma-Aldrich, P5726). Protein concentrations were quantified using BCA Protein Assay Kit (Pierce, 23225). Supernatant protein was extracted based on a chloroform-methanol protein precipitation protocol described previously (88). Extracted cell supernatant proteins and equal amount of cell lysates were separated by SDS-PAGE and transferred onto nitrocellulose membranes, followed by blocking in 5% BSA in TBST for 1 hour and incubation with indicated primary antibodies overnight. Secondary antibodies were then added and incubated for 1 hour and detection was performed using SuperSignal series West Chemiluminescent Substrate (34580/34075/34096, Thermo Fisher).

Immunofluorescent staining and confocal microscopy

For visualizing ASC speck formation, BMDMs were seeded at 2×10^5 cells/well and cultured overnight on 4-well chamber slides. The following day, cells were primed with LPS for 4 hours, pan-caspase inhibitor Z-VAD-FMK (20 μ M) was added in the LPS containing medium during the last hour, followed by treatment with inflammasome activators as indicated. The cells were fixed in 4% paraformaldehyde and blocked with 10% Power Block (HK0855K; Biogenex Laboratories). Cells were then incubated with Recombinant Alexa Fluor® 647 Anti-TMS1/ASC antibody (ab313736, Abcam) overnight at 4 °C. Chamber slides were rinsed with PBS for 5 min and mounted with ProLong Diamond Antifade Mountant with DAPI (P36971; Thermo Fisher). Slides were imaged at UTSW Quantitative Light Microscopy Core (QLMC) Facility using Zeiss LSM 880 confocal microscope. Images were processed using Zen Blue (Zeiss) at identical setting. ASC-positive cells containing specks were counted manually from randomly selected fields acquired at $\times 60$ magnifications. The percentage of speck-containing cells was calculated as the fraction of ASC-positive cells containing specks.

mtDNA neosynthesis was measured as described previously (33): BMDMs were seeded at 2×10^5 cells per well in 4-well chamber slides and rested overnight to allow proper attachment, followed by LPS priming (200 ng/ml) for 4 hours in the presence of 10 μ M EdU. The cells were then washed twice with sterile PBS and fixed in 2% paraformaldehyde (PFA) for 15 min followed by permeabilization with 0.1% Triton X-100 for 10 min. EdU staining was performed using a Click-iT EdU Microplate Assay Kit (C10637, Thermo Fisher Scientific). Briefly, BMDMs were postfixed in EdU fixative for 5 min, and equal volumes of the EdU reaction cocktail, which was made immediately before use, were added to each chamber, and incubated for 25 min. The cocktail was then removed, and BMDMs were washed three times in 1% blocking solution from the Click-iT EdU Microplate Assay Kit. Cells were then incubated with anti-HSP60 antibody overnight at 4 °C followed by fluorescence-conjugated secondary antibody for 1 hour at room temperature. Chamber slides were rinsed with PBS for 5 min and mounted with ProLong Diamond Antifade Mountant with DAPI. Slides were imaged at UTSW Quantitative Light Microscopy Core (QLMC) Facility using Zeiss LSM 980 with Airyscan 2 confocal microscope. Images were processed using Zen Blue (Zeiss) at identical setting. EdU positive cells were counted manually from randomly selected fields acquired at $\times 60$ magnifications. The percentage of cells with mtDNA replication was calculated as the fraction of EdU positive cells.

Measurement of active caspase-1 by FLICA assay

The levels of active caspase-1 were quantified using an inhibitor-based, fluorescent probe (Green Fluorescent FAM-FLICA® Caspase-1 (YVAD) Assay Kit, NC0313947, ImmunoChemistry Technologies) that specifically recognized active caspase-1 as described previously (31, 34). For in vitro experiments, macrophages were primed with LPS (100 ng/ml) followed by treatment with indicated inflammasome activators. Then the cells were washed twice with PBS and loaded with 4 μ M of FLICA FAM-YVAD-FMK for 40 min and washed twice with PBS. Cells from individual samples were transferred to 96-well plates, and fluorescence

intensity from each well was measured using a BioTek Cytation 5 cell imaging multimode plate reader (Agilent). Data were normalized to LPS-primed but NLRP3 activator-untreated controls to quantify relative levels of active caspase-1.

For caspase-1 and F4/80 staining in liver samples, formalin-fixed, OCT-embedded frozen sections were stained with 4 μM of FLICA FAM-YVAD-FMK for 1 hour followed by primary anti-mouse F4/80 antibody incubation overnight at 4°C. After washing 3 times with 0.1% PBST, the sections were then incubated with fluorescently labeled secondary antibodies for 1 hour at room temperature in the dark and DAPI was used for nuclear staining. Slides were imaged using Agilent BioTek Cytation 5 Cell Imaging Multimode Reader under Image module. Images were deconvoluted and analyzed using Fiji.

Measurement of pyroptosis

Cell pyroptosis was quantitated by assaying the activity of LDH released into cell culture supernatants using the Cytotoxicity Detection Kit (LDH) (4744926001, Sigma) according to the manufacturer's instructions.

mtDNA depletion in macrophages

BMDMs and PBMC-MDMs were maintained and differentiated in indicated culture medium as described above. To deplete mtDNA from macrophages, 1 mM sodium pyruvate (GIBCO) and 100 $\mu\text{g}/\text{mL}$ uridine (Sigma) with or without 400 ng/mL ethidium bromide (Sigma) were added in culture medium on the 4th day of cell differentiation and removed at the end of the 7th day of differentiation before cell seeding. To evaluate the depletion efficiency, total DNA was isolated and mtDNA was quantified using qPCR and normalized to nuclear *Tert* (*TERT*) gene as described above.

ddC treatment of macrophages

For ddC-mediated blockage of mtDNA neosynthesis experiments, 20 μM or 50 μM 2',3'-dideoxycytidine (ddC, Sigma) was added into FBS-free DMEM during the seeding of differentiated BMDMs. ddC remained in the culture medium overnight during cell resting and LPS priming the next day but was removed before ATP treatment.

qPCR quantification of dNTP pools

Cellular dNTPs extraction was performed according to a previously described protocol (89). Briefly, BMDMs (2×10^7 cells) were washed with cold PBS and lysed for 30 min in 200 μL ice-cold 60% (v/v) methanol. Lysates were then heated at 95°C for 3 min, followed by centrifugation at 16,000 \times g for 5 min. The supernatants were harvested and evaporated using SpeedVac (Savant, NY) with medium heat. The resultant pellets were then resuspended in 20 μL dNTP buffer (50 mM Tris-HCl, pH 8.0 and 10 mM MgCl_2) and ready to assay. For mitochondrial and cytosolic dNTPs quantification, mitochondrial and cytosolic fractions were first isolated from over 1×10^8 BMDMs using Mitochondria and Cytosol fractionation Kit (89874, Thermo Fisher Scientific). The mitochondrial pellets were then lysed for 30 min in 200 μL cold 60% methanol, followed by 3 min heating at 95°C and centrifugation at 16,000 g for 5 min at 4°C. This is to harvest the metabolites containing supernatants which was then evaporated and resuspended in 20 μL dNTP buffer as described above. The cytosolic part was mixed with pure methanol to reach the final methanol concentration of 60%, and the metabolites were extracted as described above. Quantification of dNTPs was performed according to a fluorescence-based primer extension assay as previously described (90). Reaction mixtures contained 2.5 μL cell extract or dNTP standard, 1 μL dNTP mix (2.5 mmol/L) excluding the dNTP to be assayed, 1 μL primer NDP1 (10 $\mu\text{mol}/\text{L}$), 1 μL probe (10 $\mu\text{mol}/\text{L}$), 1 μL template (10 $\mu\text{mol}/\text{L}$), 2 μL MgCl_2 (25 mmol/L), 2.5 μL 10 \times PCR Buffer II and 0.8175 μL AmpliTaq Gold DNA polymerase (ABI, N8080241), with a final volume of 25 μL . Thermal profiling and fluorescence detection

were carried out using FAM channel on CFX 96 Touch Real-Time PCR Detection system (BIO-RAD, Hercules, CA, USA). Data were collected at 30 s intervals for 15 min. The concentration of each dNTP was determined by comparison to the standard curves analyzed by linear regression and corrected to give fmol quantities for 1×10^6 cells.

High-performance liquid chromatography tandem mass spectrometry (HPLC-MS/MS)

Enough volume of LC-MS grade extraction solvent (80% (v/v) methanol in water) was prepared and kept at -80°C overnight in a polypropylene tube. On the day of experiment, heavy internal standard (MSK-A2-1.2, Cambridge Isotope Laboratories) was added to the extraction solvent and vortexed well to was aspirated from all samples after the final wash. Samples were then reach the final concentration of 0.2 μM . BMDMs (about 1×10^7 cells), ATMs (about 1×10^7 cells), and CD14⁺ monocytes (about 3×10^6 cells) were washed with cold PBS for 3 times. The excess PBS lysed in 0.5 mL of extraction solvent at -20°C for 5 min. Lysates were vortexed for 1 min at 4°C, followed by centrifugation at 14,000 g for 15 min at 4°C to pellet the cell debris. The pellet in each tube was kept for normalization of cell amount, for BMDMs and ATMs, about 1 mg protein were used as an indicator for 10 million cells, for CD14⁺ monocytes, about 350 μg protein were used as an indicator for 3 million cells, and the metabolite-containing supernatants were harvested and filtered with the 0.22 μm Ultrafree-MC Centrifugal hydrophilic PVDF Filter (SKU UFC30GVNB, Millipore) at 12,000 g for 1-4 min at 4°C. The samples were dried using a speed vac (without heat) and subsequently reconstituted in 120 μL of an 80/20 (v/v) methanol/water (LC-MS) grade solution and then transferred to glass HPLC vials and kept at -75°C prior to LC-MS analysis. HPLC-MS/MS was performed at the metabolomics core facility at UT Southwestern Medical Center. A targeted strategy was used to identify cellular dNTPs. LC-MS/MS mass spectrometric analyses were performed on a Sciex QTRAP 6500+ mass spectrometer equipped with an electrospray ion (ESI) source. The ESI source was used in the negative ion mode, configured as follows: Ion Source Gas 1 (Gas 1), 40psi; Ion Source Gas 2 (Gas 2), 35 psi; curtain gas (CUR), 50 psi; source temperature, 550°C; and ion spray voltage (IS), -4500 V (-). The mass spectrometer was coupled to a Shimadzu HPLC (Nexera X2 LC-30AD). The system is controlled by Analyst 1.7.3 software. Hydrophilic interaction chromatography was performed using a SeQuant® ZIC®-pHILIC 5 μm polymeric 150 \times 2.1 mm PEEK coated HPLC column (Millipore Sigma, USA). The column temperature, sample injection volume, and flow rate were 45°C, 2 μL , and 0.15 mL/min respectively. HPLC conditions were as follows: Solvent A: 20 mM ammonium carbonate including 0.1% Ammonium hydroxide and 5 μM of Medronic acid. Solvent B: Acetonitrile. Gradient pattern: 0 min: 80% B, 20 min: 20% B, 20.5 min 80% B, 34 min: 80% B. Each chromatography separation took 20 min, followed by additional time for column cleaning and equilibration. Data were processed using MultiQuant software with a relative quantification based on the peak area of each metabolite.

Deoxyribonucleosides supplementation

Deoxyribonucleosides (dNs) supplementation of BMDMs was performed according to previously reported studies with slight modifications (91, 92). For experimental purposes, dialyzed fetal bovine serum (dFBS, A3382001, Gibco) was used throughout the experimental procedure to maintain low exogenous nucleotide levels in the culture media. In brief, freshly isolated mouse bone marrow cells were incubated with high glucose DMEM supplemented with 10% FBS, 20% L929-cell conditioned medium, 100 U/mL penicillin-streptomycin, and a mixture of all 4 deoxyribonucleosides (dNs mix, dA/ dC/ dG/ dT) in two different concentrations (200 μM and 400 μM for each of the nucleoside separately in the mixture) for 7 days. Deoxyribonucleosides were replenished on day 4. After 7 days, cells were plated in 6-well plates with a density of 2×10^6 cells per well and incubated overnight

in FBS-free DMEM medium before inflammasome activation or mtDNA quantification.

Seahorse XFe96 respirometry

The oxygen consumption rate (OCR) was performed using the Seahorse Xfe96 Extracellular Flux analyzer (Agilent) at UTSW CRI's Metabolomics Facility. Briefly, cells were plated at 2×10^5 per well in 80 μ l of culture medium overnight in an XFe96 well plate (Seahorse Bioscience). The next day, cells were washed three times into assay media, DMEM (Sigma D5030), supplemented with 2 mM L-glutamine, 1 mM pyruvate, 10 mM glucose, and 100 U/mL penicillin/streptomycin, pH7.4, and incubated at 37°C in a CO₂-free incubator for 1 hour before starting the assay. Oxygen consumption rate (OCR) was measured in a Seahorse XFe96 instrument using consecutive three mix (3 min) and measurement (3 min) cycles. Oligomycin (final concentration 2 μ M), CCCP (final concentration 1 μ M), and antimycin A (final concentration 2 μ M) were injected as indicated.

Mouse septic shock model

Septic shock was induced by intraperitoneal injection of 8-12 weeks old, gender-matched *Samhd1*^{+/+} and *Samhd1*^{-/-} mice with LPS (*E. coli* O111:B4, Sigma-Aldrich) at 30 mg per kg body weight. Mouse survival was monitored every 6 hours after injection for a total of 72 hours. In separate experiments, mice were treated with the same dose of LPS, and sera were collected using microhematocrit tubes 3 hours post injection. Serum IL-1 β and TNF were measured by ELISA as described above. For MCC950-mediated NLRP3 inhibition, mice were intraperitoneally injected with 100 μ L MCC950 (50 mg/kg) or NaCl (0.9 g/L) 30 min before LPS injection, and serum IL-1 β and TNF were measured by ELISA.

Mouse peritonitis model

Peritonitis was induced by intraperitoneal injection of PBS or 1 mg alum (dissolved in 0.2 ml sterile PBS) into 8- to 12-week-old gender-matched *Samhd1*^{+/+} and *Samhd1*^{-/-} mice or *Cmpk2*^{+/+} and *Cmpk2*^{-/-} mice. Mice from each genotype were allocated randomly into PBS or alum treatment groups. After 12 hours, mice were euthanized by CO₂ exposure, and the peritoneal cavities were washed with 6 ml cold sterile PBS. 0.2 ml of peritoneal lavage fluid from each mouse was subjected to ELISA for mouse IL-1 β detection. For neutrophils and monocytes recruitment determination, cells were pre-incubated with 0.5–1 μ g of purified anti-mouse CD16/CD32 per 100 μ L. Isolated cells were stained with labeled antibodies in PBS with 2% FCS and 2 mM EDTA or cell staining buffer (Biolegend). Dead cells were excluded based on staining with Live/Dead fixable dye (FVD-eFluor780, eBioscience). Absolute numbers of immune cell subtypes in the peritoneum were calculated by multiplying total peritoneal cell numbers by percentages of immune cell subtypes amongst total cells. Neutrophils (CD11b⁺Ly6G⁺ F4/80⁻) and monocytes (CD11b⁺Ly6C⁺Ly6G⁻) present in the peritoneal lavage fluid were quantified by flow cytometry using a FACS LSR II flow cytometer (BD Biosciences), and data were analyzed using FlowJo software (TreeStar). For the control experiments, zymosan was used to induce peritonitis as previously described (68) by injection of 0.2 mg of zymosan in 0.5 ml sterile PBS. After 6 hours, mice were euthanized by CO₂ exposure and peritoneal cavities were washed with 6 ml cold sterile PBS. The lavage fluids were then analyzed for neutrophils and monocytes recruitment by FACS as described above.

Mouse fulminant hepatitis model

Acute liver injury was induced as previously described (93). Briefly, 8 to 12-week-old gender-matched *Samhd1*^{+/+} and *Samhd1*^{-/-} mice were intraperitoneally injected with 20 mg D-galactosamine (GalN) and 0.5 μ g LPS (*E. coli* O111: B4, Sigma-Aldrich). After 6 hours, mice were anesthetized with isoflurane, 1 ml of blood were collected

using EDTA-containing microhematocrit tubes. Plasmatic fraction may then be recovered by centrifugation (1,000 \times g, 15 min, 4°C) and analyzed for ALT enzymatic activity. Liver samples were collected for hematoxylin and eosin (H&E) staining and immunofluorescent co-staining of active caspase-1 (FAM-FLICA® Caspase-1 (YVAD) Assay Kit, NC0313947, ImmunoChemistry Technologies) and F4/80 (Anti-mouse F4/80 BV421 (clone BM8)).

Mouse HFD model

Samhd1^{+/+}, *Samhd1*^{-/-}, *Samhd1*^{F/F}, *Samhd1* ^{Δ Myc}, *Cmpk2*^{+/+}, *Cmpk2*^{-/-}, and wild-type C57BL/6 mice, 6–7 weeks of age, were fed with a normal diet (ND) or a high-fat diet (HFD) in which 60% of calories derived from saturated fat (S3282; Bio-Serv) for 24 weeks and had free access to water and food. Mice were fed and weighed every week on the same day. Lean and fat body mass were evaluated using an EchoMRI-100 (Echo Medical Systems) at UTSW's Metabolic Phenotyping Core facility. GTT and ITT were conducted after HFD feeding for 12 and 13 weeks, respectively, as described previously (25). For GTT, the mice were fasted overnight (~16 hours). At 9:00 the next morning, mice were injected intraperitoneally with glucose solution at a dosage of 1 g/kg body weight. For ITT, the mice were fasted for 6 hours. Mice were injected intraperitoneally with insulin solution at a dosage of 1 IU/kg. Blood glucose was measured using a FreeStyle Lite glucometer (AlphaTrak, Abbott). For quantification of serum cytokines, retro-orbital blood was drawn at the end of the 14th, 19th week of HFD feeding, and whole blood was drawn at the end of 24th week when the mice were euthanized. Serum was collected for the quantification of circulating IL-1 β and TNF levels by ELISA as well as metabolic phenotyping for serum alanine transaminase (ALT), aspartate aminotransferase (AST), total cholesterol (TC), and total triglyceride (TG) analysis as described previously (27). Liver and eWAT samples were collected for histology, RNA extraction and protein extraction for further analyses.

Liver histology

Fresh mouse liver tissues were collected and fixed with formalin and then embedded with paraffin or OCT compound. The paraffin sections were stained with H&E for assessment of liver histology, and Sirius Red (Sigma, 365548)/Fast Green (Sigma, F258) for assessment of fibrosis. The frozen sections were used for Oil-Red O staining. The images with H&E and Oil-Red O staining were processed using a Cytation 5 Cell Imaging Multimode Reader (BioTek). The images with Sirius Red/Fast Green staining were detected using a Zeiss AxioScope (Zeiss, CA, USA) under polarized light.

Zebrafish study

Zebrafish work described in this study was approved and conducted under the oversight of the UT Southwestern Institutional Animal Care and Use Committee. All embryos were maintained at 28.5°C throughout development and experiments. All zebrafish experiments were performed at the embryonic stage and therefore the sex of embryo was not yet determined. The *samhd1* mutant line was generated using the CRISPR/Cas9 system. The sgRNA targeting exon4 of *samhd1* (target site: GAACCTACCTGGTGTTCCTCCCGGG) was synthesized with the MEGAscript T7 Transcription Kit (Invitrogen) and purified through LiCl precipitation (Invitrogen). One hundred embryos were injected at the one-cell stage with a mixture of 100 pg sgRNA and 500 pg Cas9 protein (PNA Bio). Ten embryos were randomly collected to evaluate the targeting efficiency by BstNI digestion after PCR (genotyping primers: forward primer: 5'-TTGAGTGTCTTGTGGACGG-3', reverse primer: 5'-GCAGTTCTCAGACTGGAAGG-3'). Each F0 founder fish was outcrossed with wild type to obtain heterozygous F1s. Heterozygous F1s were sequenced and then crossed to generate homozygous mutants. Two *samhd1* mutant lines (-10bp-/- and -11bp-/-) were obtained and used for experiments. Sequence information of the -10bp and -11bp alleles. GAACCTACCTGGTGTTCCTCCCGGG (WT); GAACCTA—CCCGGG

(-10bp); GAACCTA—CCGGG (-11bp). In vivo induction and detection of DrNLRP3 inflammasome was performed in zebrafish embryos as previously described (94). In brief, *samhd1*^{+/+} and *samhd1*^{-/-} zebrafish embryos (over 200 embryos per group) were collected at 72 hours post-fertilization (hpf). To activate DrNLRP3 inflammasome in vivo, the embryos were immersed in 10 mM H₂O₂ (H1009, Sigma) in a 10 cm dish for 40 min, and then collected for protein extraction. DrIL-1 β maturation was determined using immunoblotting as described above. DrCaspase A and B activation was detected using Caspase assay with fluorogenic substrates. Briefly, the embryos (about 25 embryos per group unless otherwise noticed) were harvested and lysed in 100 μ L caspase cell lysis buffer (Enzo Life Sciences). 100 μ g Lysate protein was added to the caspase assay buffer (Enzo Life Sciences) containing 100 μ M acetyl-Tyr-Val-Ala-Asp-amido-4-trifluoromethylcoumarin (Ac-YVAD-AFC, specific to DrCaspase-A, Alexis, San Diego, CA) or Ac-Trp-Glu-His-Asp-AFC (Ac-WEHD-AFC, specific to DrCaspase-B) (Alexis, San Diego, CA) as described previously (94). For Fig. 2Z, each larva was harvested separately in 5 μ L caspase cell lysis buffer (Enzo Life Sciences). 5 μ g Lysate protein was added to the caspase assay buffer containing 100 μ M Ac-YVAD-AFC. After incubation at 37°C for 2 hours, the cleavage of caspase-type-specific substrate emitted a fluorescent signal that was measured with excitation at 400 nm and emission at 505 nm on a Biotek Cytation 5 multimode plate reader (Agilent). EB depletion of zebrafish mtDNA was performed according to a previously published study (95). In brief, large numbers (over 400 per group) of 3 hpf zebrafish embryos were exposed to 15 μ g/ml ethidium bromide (EtBr, EMD chemicals) for 6 days. At 72 hpf, media was removed and fresh embryo media with EtBr was added. After 6 days, all media was removed, and larvae were washed three times with fresh embryo media without EtBr before the inflammasome induction or mtDNA quantification. Zebrafish mtDNA quantification (about 15-20 larvae per group) was performed using QIAamp DNA Mini Kit (250) (51306, QIAGEN) according to manufacturer's instructions. mtDNA was quantified by qPCR using primers specific for the mitochondrial NADH dehydrogenase subunit 1 gene (*nd1*). Nuclear DNA encoding *B2m* was used for normalization. Primer sequences are as follows: *nd1* F: 5'-CCACTTAATTAACCCCTAGCC3'; *nd1* R: 5'-ATGTTTGTTGGGGGTAGACCA-3'; *b2m* F: 5'-CGCCTGAAAACACTACGTTCTACAC-3'; *b2m* R: 5'-ACTTTCGGAGTGGCTGAAAA-3';

Statistics

Statistical analyses as described in the figure legends were performed either using Microsoft Excel or GraphPad Prism (GraphPad, www.graphpad.com). All data are mean \pm SD or mean \pm SEM as indicated. Statistical analysis was performed using a two-tailed unpaired Student's *t* test, one-way analysis of variance (ANOVA) test, two-way ANOVA test or log-rank test (for survival analysis). For all tests, *P* < 0.05 was considered statistically significant. No statistical methods were used to predetermine the sample size. Sample sizes were chosen to ensure adequate power and to account for potential interindividual/animal, gender, and age variance (age- and sex-matched samples were used as controls). The experiments were not randomized except for the in vivo studies in which the age- and gender-matched mice were randomly allocated to different experimental groups based on their genotypes. Investigators were not blinded to allocation during experiments and outcome assessment except for microscopic analysis of immunofluorescent staining results.

REFERENCES AND NOTES

- D. W. Haslam, W. P. James, Obesity. *Lancet* **366**, 1197–1209 (2005). doi: [10.1016/S0140-6736\(05\)67483-1](https://doi.org/10.1016/S0140-6736(05)67483-1); pmid: [16198769](https://pubmed.ncbi.nlm.nih.gov/16198769/)
- H. Rodríguez-Hernández, L. E. Simental-Mendía, G. Rodríguez-Ramírez, M. A. Reyes-Romero, Obesity and inflammation: Epidemiology, risk factors, and markers of inflammation. *Int. J. Endocrinol.* **2013**, 678159 (2013). doi: [10.1155/2013/678159](https://doi.org/10.1155/2013/678159); pmid: [23690772](https://pubmed.ncbi.nlm.nih.gov/23690772/)
- P. L. Valenzuela et al., Obesity and the risk of cardiometabolic diseases. *Nat. Rev. Cardiol.* **20**, 475–494 (2023). doi: [10.1038/s41569-023-00847-5](https://doi.org/10.1038/s41569-023-00847-5); pmid: [36927772](https://pubmed.ncbi.nlm.nih.gov/36927772/)
- T. L. Visscher, J. C. Seidell, The public health impact of obesity. *Annu. Rev. Public Health* **22**, 355–375 (2001). doi: [10.1146/annurev.publhealth.22.1.355](https://doi.org/10.1146/annurev.publhealth.22.1.355); pmid: [11274526](https://pubmed.ncbi.nlm.nih.gov/11274526/)
- P. J. Goodwin, V. Stambolic, Impact of the obesity epidemic on cancer. *Annu. Rev. Med.* **66**, 281–296 (2015). doi: [10.1146/annurev-med-051613-012328](https://doi.org/10.1146/annurev-med-051613-012328); pmid: [25423596](https://pubmed.ncbi.nlm.nih.gov/25423596/)
- Y. Wang, M. A. Beydoun, L. Liang, B. Caballero, S. K. Kumanyika, Will all Americans become overweight or obese? estimating the progression and cost of the US obesity epidemic. *Obesity (Silver Spring)* **16**, 2323–2330 (2008). doi: [10.1038/oby.2008.351](https://doi.org/10.1038/oby.2008.351); pmid: [18719634](https://pubmed.ncbi.nlm.nih.gov/18719634/)
- M. Y. Donath, É. Dalmás, N. S. Sauter, M. Böni-Schnetzler, Inflammation in obesity and diabetes: Islet dysfunction and therapeutic opportunity. *Cell Metab.* **17**, 860–872 (2013). doi: [10.1016/j.cmet.2013.05.001](https://doi.org/10.1016/j.cmet.2013.05.001); pmid: [23747245](https://pubmed.ncbi.nlm.nih.gov/23747245/)
- Y. Ma, O. Ajnakina, A. Steptoe, D. Cadar, Higher risk of dementia in English older individuals who are overweight or obese. *Int. J. Epidemiol.* **49**, 1353–1365 (2020). doi: [10.1093/ije/dyaa099](https://doi.org/10.1093/ije/dyaa099); pmid: [32575116](https://pubmed.ncbi.nlm.nih.gov/32575116/)
- J. A. Flores-Cordero et al., Obesity as a Risk Factor for Dementia and Alzheimer's Disease: The Role of Leptin. *Int. J. Mol. Sci.* **23**, 5202 (2022). doi: [10.3390/ijms23095202](https://doi.org/10.3390/ijms23095202); pmid: [35563589](https://pubmed.ncbi.nlm.nih.gov/35563589/)
- B. Sun, M. Karin, Obesity, inflammation, and liver cancer. *J. Hepatol.* **56**, 704–713 (2012). doi: [10.1016/j.jhep.2011.09.020](https://doi.org/10.1016/j.jhep.2011.09.020); pmid: [22120206](https://pubmed.ncbi.nlm.nih.gov/22120206/)
- S. P. Bapat et al., Obesity alters pathology and treatment response in inflammatory disease. *Nature* **604**, 337–342 (2022). doi: [10.1038/s41586-022-04536-0](https://doi.org/10.1038/s41586-022-04536-0); pmid: [35355021](https://pubmed.ncbi.nlm.nih.gov/35355021/)
- T. V. Rohm, D. T. Meier, J. M. Olefsky, M. Y. Donath, Inflammation in obesity, diabetes, and related disorders. *Immunity* **55**, 31–55 (2022). doi: [10.1016/j.immuni.2021.12.013](https://doi.org/10.1016/j.immuni.2021.12.013); pmid: [35021057](https://pubmed.ncbi.nlm.nih.gov/35021057/)
- M. Y. Donath, C. A. Dinarello, T. Mandrup-Poulsen, Targeting innate immune mediators in type 1 and type 2 diabetes. *Nat. Rev. Immunol.* **19**, 734–746 (2019). doi: [10.1038/s41577-019-0213-9](https://doi.org/10.1038/s41577-019-0213-9); pmid: [31501536](https://pubmed.ncbi.nlm.nih.gov/31501536/)
- A. R. Saltiel, J. M. Olefsky, Inflammatory mechanisms linking obesity and metabolic disease. *J. Clin. Invest.* **127**, 1–4 (2017). doi: [10.1172/JCI92035](https://doi.org/10.1172/JCI92035); pmid: [28045402](https://pubmed.ncbi.nlm.nih.gov/28045402/)
- S. M. Reilly, A. R. Saltiel, Adapting to obesity with adipose tissue inflammation. *Nat. Rev. Endocrinol.* **13**, 633–643 (2017). doi: [10.1038/nrendo.2017.90](https://doi.org/10.1038/nrendo.2017.90); pmid: [28799554](https://pubmed.ncbi.nlm.nih.gov/28799554/)
- F. Zhong, S. Liang, Z. Zhong, Emerging Role of Mitochondrial DNA as a Major Driver of Inflammation and Disease Progression. *Trends Immunol.* **40**, 1120–1133 (2019). doi: [10.1016/j.it.2019.10.008](https://doi.org/10.1016/j.it.2019.10.008); pmid: [31744765](https://pubmed.ncbi.nlm.nih.gov/31744765/)
- Z. Zhong, E. Sanchez-Lopez, M. Karin, Autophagy, Inflammation, and Immunity: A Troika Governing Cancer and Its Treatment. *Cell* **166**, 288–298 (2016). doi: [10.1016/j.cell.2016.05.051](https://doi.org/10.1016/j.cell.2016.05.051); pmid: [27419869](https://pubmed.ncbi.nlm.nih.gov/27419869/)
- B. R. Sharma, T. D. Kanneganti, NLRP3 inflammasome in cancer and metabolic diseases. *Nat. Immunol.* **22**, 550–559 (2021). doi: [10.1038/s41590-021-00886-5](https://doi.org/10.1038/s41590-021-00886-5); pmid: [33707781](https://pubmed.ncbi.nlm.nih.gov/33707781/)
- K. V. Swanson, M. Deng, J. P. Ting, The NLRP3 inflammasome: Molecular activation and regulation to therapeutics. *Nat. Rev. Immunol.* **19**, 477–489 (2019). doi: [10.1038/s41577-019-0165-0](https://doi.org/10.1038/s41577-019-0165-0); pmid: [31036962](https://pubmed.ncbi.nlm.nih.gov/31036962/)
- E. L. Mills, B. Kelly, L. A. J. O'Neill, Mitochondria are the powerhouses of immunity. *Nat. Immunol.* **18**, 488–498 (2017). doi: [10.1038/nri.3704](https://doi.org/10.1038/nri.3704); pmid: [28418387](https://pubmed.ncbi.nlm.nih.gov/28418387/)
- L. Broderick, D. De Nardo, B. S. Franklin, H. M. Hoffman, E. Latz, The inflammasomes and autoinflammatory syndromes. *Annu. Rev. Pathol.* **10**, 395–424 (2015). doi: [10.1146/annurev-pathol-012414-040431](https://doi.org/10.1146/annurev-pathol-012414-040431); pmid: [25423351](https://pubmed.ncbi.nlm.nih.gov/25423351/)
- P. Broz, V. M. Dixit, Inflammasomes: Mechanism of assembly, regulation and signalling. *Nat. Rev. Immunol.* **16**, 407–420 (2016). doi: [10.1038/nri.2016.58](https://doi.org/10.1038/nri.2016.58); pmid: [27291964](https://pubmed.ncbi.nlm.nih.gov/27291964/)
- E. Latz, T. S. Xiao, A. Stutz, Activation and regulation of the inflammasomes. *Nat. Rev. Immunol.* **13**, 397–411 (2013). doi: [10.1038/nri3452](https://doi.org/10.1038/nri3452); pmid: [23702978](https://pubmed.ncbi.nlm.nih.gov/23702978/)
- M. Lamkanfi, V. M. Dixit, Mechanisms and functions of inflammasomes. *Cell* **157**, 1013–1022 (2014). doi: [10.1016/j.cell.2014.04.007](https://doi.org/10.1016/j.cell.2014.04.007); pmid: [24855941](https://pubmed.ncbi.nlm.nih.gov/24855941/)
- H. Wen et al., Fatty acid-induced NLRP3-ASC inflammasome activation interferes with insulin signaling. *Nat. Immunol.* **12**, 408–415 (2011). doi: [10.1038/ni.2022](https://doi.org/10.1038/ni.2022); pmid: [21478880](https://pubmed.ncbi.nlm.nih.gov/21478880/)
- B. Vandanmagsar et al., The NLRP3 inflammasome instigates obesity-induced inflammation and insulin resistance. *Nat. Med.* **17**, 179–188 (2011). doi: [10.1038/nm.2279](https://doi.org/10.1038/nm.2279); pmid: [21217695](https://pubmed.ncbi.nlm.nih.gov/21217695/)
- X. Wang et al., Prolonged hypernutrition impairs TREM2-dependent efferocytosis to license chronic liver inflammation and NASH development. *Immunity* **56**, 58–77.e11 (2023). doi: [10.1016/j.immuni.2022.11.013](https://doi.org/10.1016/j.immuni.2022.11.013); pmid: [36521495](https://pubmed.ncbi.nlm.nih.gov/36521495/)
- A. Esparza-Baquer et al., TREM-2 defends the liver against hepatocellular carcinoma through multifactorial protective mechanisms. *Gut* **70**, 1345–1361 (2021). doi: [10.1136/gutjnl-2019-319227](https://doi.org/10.1136/gutjnl-2019-319227); pmid: [32907830](https://pubmed.ncbi.nlm.nih.gov/32907830/)
- I. Liebold et al., TREM2 Regulates the Removal of Apoptotic Cells and Inflammatory Processes during the Progression of NAFLD. *Cells* **12**, 341 (2023). doi: [10.3390/cells12030341](https://doi.org/10.3390/cells12030341); pmid: [36766683](https://pubmed.ncbi.nlm.nih.gov/36766683/)
- K. Nakahira et al., Autophagy proteins regulate innate immune responses by inhibiting the release of mitochondrial DNA mediated by the NALP3 inflammasome. *Nat. Immunol.* **12**, 222–230 (2011). doi: [10.1038/ni.1980](https://doi.org/10.1038/ni.1980); pmid: [21151103](https://pubmed.ncbi.nlm.nih.gov/21151103/)
- K. Shimada et al., Oxidized mitochondrial DNA activates the NLRP3 inflammasome during apoptosis. *Immunity* **36**, 401–414 (2012). doi: [10.1016/j.immuni.2012.01.009](https://doi.org/10.1016/j.immuni.2012.01.009); pmid: [22342844](https://pubmed.ncbi.nlm.nih.gov/22342844/)
- A. P. West, G. S. Shadel, Mitochondrial DNA in innate immune responses and inflammatory pathology. *Nat. Rev. Immunol.* **17**, 363–375 (2017). doi: [10.1038/nri.2017.21](https://doi.org/10.1038/nri.2017.21); pmid: [28393922](https://pubmed.ncbi.nlm.nih.gov/28393922/)

33. Z. Zhong *et al.*, New mitochondrial DNA synthesis enables NLRP3 inflammasome activation. *Nature* **560**, 198–203 (2018). doi: [10.1038/s41586-018-0372-z](https://doi.org/10.1038/s41586-018-0372-z); pmid: [30046112](https://pubmed.ncbi.nlm.nih.gov/30046112/)
34. Z. Zhong *et al.*, NF- κ B Restricts Inflammasome Activation via Elimination of Damaged Mitochondria. *Cell* **164**, 896–910 (2016). doi: [10.1016/j.cell.2015.12.057](https://doi.org/10.1016/j.cell.2015.12.057); pmid: [26919428](https://pubmed.ncbi.nlm.nih.gov/26919428/)
35. R. Zhou, A. S. Yazdi, P. Menu, J. Tschopp, A role for mitochondria in NLRP3 inflammasome activation. *Nature* **469**, 221–225 (2011). doi: [10.1038/nature09663](https://doi.org/10.1038/nature09663); pmid: [21124315](https://pubmed.ncbi.nlm.nih.gov/21124315/)
36. L. K. Billingham *et al.*, Mitochondrial electron transport chain is necessary for NLRP3 inflammasome activation. *Nat. Immunol.* **23**, 692–704 (2022). doi: [10.1038/s41590-022-01185-3](https://doi.org/10.1038/s41590-022-01185-3); pmid: [35484407](https://pubmed.ncbi.nlm.nih.gov/35484407/)
37. H. Xian *et al.*, Oxidized DNA fragments exit mitochondria via mPTP- and VDAC-dependent channels to activate NLRP3 inflammasome and interferon signaling. *Immunity* **55**, 1370–1385.e8 (2022). doi: [10.1016/j.immuni.2022.06.007](https://doi.org/10.1016/j.immuni.2022.06.007); pmid: [35835107](https://pubmed.ncbi.nlm.nih.gov/35835107/)
38. H. Xian *et al.*, Metformin inhibition of mitochondrial ATP and DNA synthesis abrogates NLRP3 inflammasome activation and pulmonary inflammation. *Immunity* **54**, 1463–1477.e11 (2021). doi: [10.1016/j.immuni.2021.05.004](https://doi.org/10.1016/j.immuni.2021.05.004); pmid: [34115964](https://pubmed.ncbi.nlm.nih.gov/34115964/)
39. S. H. Baik *et al.*, Hexokinase dissociation from mitochondria promotes oligomerization of VDAC that facilitates NLRP3 inflammasome assembly and activation. *Sci. Immunol.* **8**, eade7652 (2023). doi: [10.1126/sciimmunol.ade7652](https://doi.org/10.1126/sciimmunol.ade7652); pmid: [37327321](https://pubmed.ncbi.nlm.nih.gov/37327321/)
40. T. Misawa *et al.*, Microtubule-driven spatial arrangement of mitochondria promotes activation of the NLRP3 inflammasome. *Nat. Immunol.* **14**, 454–460 (2013). doi: [10.1038/ni.2550](https://doi.org/10.1038/ni.2550); pmid: [23502856](https://pubmed.ncbi.nlm.nih.gov/23502856/)
41. M. P. Murphy, L. A. J. O'Neill, A break in mitochondrial endosymbiosis as a basis for inflammatory diseases. *Nature* **626**, 271–279 (2024). doi: [10.1038/s41586-023-06866-z](https://doi.org/10.1038/s41586-023-06866-z); pmid: [38326590](https://pubmed.ncbi.nlm.nih.gov/38326590/)
42. J. Rius *et al.*, NF- κ B links innate immunity to the hypoxic response through transcriptional regulation of HIF-1 α . *Nature* **453**, 807–811 (2008). doi: [10.1038/nature06905](https://doi.org/10.1038/nature06905); pmid: [18432192](https://pubmed.ncbi.nlm.nih.gov/18432192/)
43. S. Li *et al.*, SFTSV Infection Induces BAK/BAX-Dependent Mitochondrial DNA Release to Trigger NLRP3 Inflammasome Activation. *Cell Rep.* **30**, 4370–4385.e7 (2020). doi: [10.1016/j.celrep.2020.02.105](https://doi.org/10.1016/j.celrep.2020.02.105); pmid: [32234474](https://pubmed.ncbi.nlm.nih.gov/32234474/)
44. A. Cabral *et al.*, Differential Binding of NLRP3 to non-oxidized and Ox-mtDNA mediates NLRP3 Inflammasome Activation. *Commun. Biol.* **6**, 578 (2023). doi: [10.1038/s42003-023-04817-y](https://doi.org/10.1038/s42003-023-04817-y); pmid: [37253813](https://pubmed.ncbi.nlm.nih.gov/37253813/)
45. K. K. L. Wu *et al.*, The APPL1-Rab5 axis restricts NLRP3 inflammasome activation through early endosomal-dependent mitophagy in macrophages. *Nat. Commun.* **12**, 6637 (2021). doi: [10.1038/s41467-021-26987-1](https://doi.org/10.1038/s41467-021-26987-1); pmid: [34789781](https://pubmed.ncbi.nlm.nih.gov/34789781/)
46. E. Ballana, J. A. Esté, SAMHD1: At the crossroads of cell proliferation, immune responses, and virus restriction. *Trends Microbiol.* **23**, 680–692 (2015). doi: [10.1016/j.tim.2015.08.002](https://doi.org/10.1016/j.tim.2015.08.002); pmid: [26439297](https://pubmed.ncbi.nlm.nih.gov/26439297/)
47. S. Chen, S. Bonifati, Z. Qin, C. St Gelais, L. Wu, SAMHD1 Suppression of Antiviral Immune Responses. *Trends Microbiol.* **27**, 254–267 (2019). doi: [10.1016/j.tim.2018.09.009](https://doi.org/10.1016/j.tim.2018.09.009); pmid: [30336972](https://pubmed.ncbi.nlm.nih.gov/30336972/)
48. B. Orris *et al.*, Phosphorylation of SAMHD1 Thr592 increases C-terminal domain dynamics, tetramer dissociation and ssDNA binding kinetics. *Nucleic Acids Res.* **50**, 7545–7559 (2022). doi: [10.1093/nar/gkac573](https://doi.org/10.1093/nar/gkac573); pmid: [35801923](https://pubmed.ncbi.nlm.nih.gov/35801923/)
49. D. C. Goldstone *et al.*, HIV-1 restriction factor SAMHD1 is a deoxynucleoside triphosphate triphosphohydrolase. *Nature* **480**, 379–382 (2011). doi: [10.1038/nature10623](https://doi.org/10.1038/nature10623); pmid: [22506990](https://pubmed.ncbi.nlm.nih.gov/22506990/)
50. L. M. Koharudin *et al.*, Structural basis of allosteric activation of sterile α motif and histidine-aspartate domain-containing protein 1 (SAMHD1) by nucleoside triphosphates. *J. Biol. Chem.* **289**, 32617–32627 (2014). doi: [10.1074/jbc.M114.591958](https://doi.org/10.1074/jbc.M114.591958); pmid: [25288794](https://pubmed.ncbi.nlm.nih.gov/25288794/)
51. L. H. Arnold *et al.*, Phospho-dependent Regulation of SAMHD1 Oligomerisation Couples Catalysis and Restriction. *PLoS Pathog.* **11**, e1005194 (2015). doi: [10.1371/journal.ppat.1005194](https://doi.org/10.1371/journal.ppat.1005194); pmid: [26431200](https://pubmed.ncbi.nlm.nih.gov/26431200/)
52. J. Deutschmann, T. Gramberg, SAMHD1 ... and Viral Ways around It. *Viruses* **13**, 395 (2021). doi: [10.3390/v13030395](https://doi.org/10.3390/v13030395); pmid: [33801276](https://pubmed.ncbi.nlm.nih.gov/33801276/)
53. N. E. Bowen *et al.*, Structural and functional characterization explains loss of dNTPase activity of the cancer-specific R366C/H mutant SAMHD1 proteins. *J. Biol. Chem.* **297**, 101170 (2021). doi: [10.1016/j.jbc.2021.101170](https://doi.org/10.1016/j.jbc.2021.101170); pmid: [34492268](https://pubmed.ncbi.nlm.nih.gov/34492268/)
54. M. Malumbres, M. Barbacid, Cell cycle, CDKs and cancer: A changing paradigm. *Nat. Rev. Cancer* **9**, 153–166 (2009). doi: [10.1038/nrc2602](https://doi.org/10.1038/nrc2602); pmid: [19238148](https://pubmed.ncbi.nlm.nih.gov/19238148/)
55. A. D. Wells, P. A. Morawski, New roles for cyclin-dependent kinases in T cell biology: Linking cell division and differentiation. *Nat. Rev. Immunol.* **14**, 261–270 (2014). doi: [10.1038/nri3625](https://doi.org/10.1038/nri3625); pmid: [24603166](https://pubmed.ncbi.nlm.nih.gov/24603166/)
56. E. Pauls *et al.*, Cell cycle control and HIV-1 susceptibility are linked by CDK6-dependent CDK2 phosphorylation of SAMHD1 in myeloid and lymphoid cells. *J. Immunol.* **193**, 1988–1997 (2014). doi: [10.4049/jimmunol.1400873](https://doi.org/10.4049/jimmunol.1400873); pmid: [25015816](https://pubmed.ncbi.nlm.nih.gov/25015816/)
57. E. Pauls *et al.*, p21 regulates the HIV-1 restriction factor SAMHD1. *Proc. Natl. Acad. Sci. U.S.A.* **111**, E1322–E1324 (2014). doi: [10.1073/pnas.1322059111](https://doi.org/10.1073/pnas.1322059111); pmid: [24610778](https://pubmed.ncbi.nlm.nih.gov/24610778/)
58. K. Schott *et al.*, Dephosphorylation of the HIV-1 restriction factor SAMHD1 is mediated by PP2A-B5 α holoenzymes during mitotic exit. *Nat. Commun.* **9**, 2227 (2018). doi: [10.1038/s41467-018-04671-1](https://doi.org/10.1038/s41467-018-04671-1); pmid: [29884836](https://pubmed.ncbi.nlm.nih.gov/29884836/)
59. J. Yan *et al.*, CyclinA2-Cyclin-dependent Kinase Regulates SAMHD1 Protein Phosphohydrolase Domain. *J. Biol. Chem.* **290**, 13279–13292 (2015). doi: [10.1074/jbc.M115.646588](https://doi.org/10.1074/jbc.M115.646588); pmid: [25847232](https://pubmed.ncbi.nlm.nih.gov/25847232/)
60. M. C. Tsai *et al.*, Attenuation of reverse transcriptase facilitates SAMHD1 restriction of HIV-1 in cycling cells. *Retrovirology* **20**, 5 (2023). doi: [10.1186/s12977-023-00620-z](https://doi.org/10.1186/s12977-023-00620-z); pmid: [37127613](https://pubmed.ncbi.nlm.nih.gov/37127613/)
61. C. Tang, X. Ji, L. Wu, Y. Xiong, Impaired dNTPase activity of SAMHD1 by phosphomimetic mutation of Thr-592. *J. Biol. Chem.* **290**, 26352–26359 (2015). doi: [10.1074/jbc.M115.677435](https://doi.org/10.1074/jbc.M115.677435); pmid: [26294762](https://pubmed.ncbi.nlm.nih.gov/26294762/)
62. C. K. J. Young, J. H. Wheeler, M. M. Rahman, M. J. Young, The antiretroviral 2',3'-dideoxycytidine causes mitochondrial dysfunction in proliferating and differentiated HepaRG human cell cultures. *J. Biol. Chem.* **296**, 100206 (2021). doi: [10.1074/jbc.RA120.014885](https://doi.org/10.1074/jbc.RA120.014885); pmid: [33334881](https://pubmed.ncbi.nlm.nih.gov/33334881/)
63. S. U. Lyanage *et al.*, Leveraging increased cytoplasmic nucleoside kinase activity to target mtDNA and oxidative phosphorylation in AML. *Blood* **129**, 2657–2666 (2017). doi: [10.1182/blood-2016-10-741207](https://doi.org/10.1182/blood-2016-10-741207); pmid: [28283480](https://pubmed.ncbi.nlm.nih.gov/28283480/)
64. C. Blázquez-Bermejo *et al.*, Increased dNTP pools rescue mtDNA depletion in human POLG-deficient fibroblasts. *FASEB J.* **33**, 7168–7179 (2019). doi: [10.1096/fj.2018015919](https://doi.org/10.1096/fj.2018015919); pmid: [30848931](https://pubmed.ncbi.nlm.nih.gov/30848931/)
65. N. Kayagaki *et al.*, Caspase-11 cleaves gasdermin D for non-canonical inflammasome signalling. *Nature* **526**, 666–671 (2015). doi: [10.1038/nature15541](https://doi.org/10.1038/nature15541); pmid: [26375259](https://pubmed.ncbi.nlm.nih.gov/26375259/)
66. J. Shi *et al.*, Inflammasome caspases are innate immune receptors for intracellular LPS. *Nature* **514**, 187–192 (2014). doi: [10.1038/nature13683](https://doi.org/10.1038/nature13683); pmid: [25119034](https://pubmed.ncbi.nlm.nih.gov/25119034/)
67. N. Subramanian, K. Natarajan, M. R. Clatworthy, Z. Wang, R. N. Germain, The adaptor MAVS promotes NLRP3 mitochondrial localization and inflammasome activation. *Cell* **153**, 348–361 (2013). doi: [10.1016/j.cell.2013.02.054](https://doi.org/10.1016/j.cell.2013.02.054); pmid: [23582325](https://pubmed.ncbi.nlm.nih.gov/23582325/)
68. F. Martinon, V. Pétrilli, A. Mayor, A. Tardivel, J. Tschopp, Gout-associated uric acid crystals activate the NALP3 inflammasome. *Nature* **440**, 237–241 (2006). doi: [10.1038/nature04516](https://doi.org/10.1038/nature04516); pmid: [16407889](https://pubmed.ncbi.nlm.nih.gov/16407889/)
69. A. Christ, M. Lauterbach, E. Latz, Western Diet and the Immune System: An Inflammatory Connection. *Immunity* **51**, 794–811 (2019). doi: [10.1016/j.immuni.2019.09.020](https://doi.org/10.1016/j.immuni.2019.09.020); pmid: [31747581](https://pubmed.ncbi.nlm.nih.gov/31747581/)
70. Y. Xu, M. Johansson, A. Karlsson, Human UMP-CMP kinase 2, a novel nucleoside monophosphate kinase localized in mitochondria. *J. Biol. Chem.* **283**, 1563–1571 (2008). doi: [10.1074/jbc.M707997200](https://doi.org/10.1074/jbc.M707997200); pmid: [17999954](https://pubmed.ncbi.nlm.nih.gov/17999954/)
71. Y. Liu, X. Lu, X. Li, P. Du, G. Qin, High-fat diet triggers obesity-related early infiltration of macrophages into adipose tissue and transient reduction of blood monocyte count. *Mol. Immunol.* **117**, 139–146 (2020). doi: [10.1016/j.molimm.2019.11.002](https://doi.org/10.1016/j.molimm.2019.11.002); pmid: [31778913](https://pubmed.ncbi.nlm.nih.gov/31778913/)
72. S. P. Weisberg *et al.*, Obesity is associated with macrophage accumulation in adipose tissue. *J. Clin. Invest.* **112**, 1796–1808 (2003). doi: [10.1172/JCI200319246](https://doi.org/10.1172/JCI200319246); pmid: [14679176](https://pubmed.ncbi.nlm.nih.gov/14679176/)
73. A. Remmerie *et al.*, Osteopontin Expression Identifies a Subset of Recruited Macrophages Distinct from Kupffer Cells in the Fatty Liver. *Immunity* **53**, 641–657.e14 (2020). doi: [10.1016/j.immuni.2020.08.004](https://doi.org/10.1016/j.immuni.2020.08.004); pmid: [32888418](https://pubmed.ncbi.nlm.nih.gov/32888418/)
74. J. S. Seidman *et al.*, Niche-Specific Reprogramming of Epigenetic Landscapes Drives Myeloid Cell Diversity in Nonalcoholic Steatohepatitis. *Immunity* **52**, 1057–1074.e7 (2020). doi: [10.1016/j.immuni.2020.04.001](https://doi.org/10.1016/j.immuni.2020.04.001); pmid: [32362324](https://pubmed.ncbi.nlm.nih.gov/32362324/)
75. M. M. Mehta, S. E. Weinberg, N. S. Chandel, Mitochondrial control of immunity: Beyond ATP. *Nat. Rev. Immunol.* **17**, 608–620 (2017). doi: [10.1038/nri.2017.66](https://doi.org/10.1038/nri.2017.66); pmid: [28669986](https://pubmed.ncbi.nlm.nih.gov/28669986/)
76. H. G. Sprenger *et al.*, Cellular pyrimidine imbalance triggers mitochondrial DNA-dependent innate immunity. *Nat. Metab.* **3**, 636–650 (2021). doi: [10.1038/s42255-021-00385-9](https://doi.org/10.1038/s42255-021-00385-9); pmid: [33903774](https://pubmed.ncbi.nlm.nih.gov/33903774/)
77. F. Coquel, C. Neumayer, Y. L. Lin, P. Pasero, SAMHD1 and the innate immune response to cytosolic DNA during DNA replication. *Curr. Opin. Immunol.* **56**, 24–30 (2019). doi: [10.1016/j.coi.2018.09.017](https://doi.org/10.1016/j.coi.2018.09.017); pmid: [30292848](https://pubmed.ncbi.nlm.nih.gov/30292848/)
78. A. Liu, S. Ying, Aicardi-Goutières syndrome: A monogenic type I interferonopathy. *Scand. J. Immunol.* **98**, e13314 (2023). doi: [10.1111/sji.13314](https://doi.org/10.1111/sji.13314); pmid: [37515439](https://pubmed.ncbi.nlm.nih.gov/37515439/)
79. S. Maharana *et al.*, SAMHD1 controls innate immunity by regulating condensation of immunogenetic self RNA. *Mol. Cell* **82**, 3712–3728.e10 (2022). doi: [10.1016/j.molcel.2022.08.031](https://doi.org/10.1016/j.molcel.2022.08.031); pmid: [36150385](https://pubmed.ncbi.nlm.nih.gov/36150385/)
80. T. Schumann *et al.*, Deficiency for SAMHD1 activates MDA5 in a cGAS/STING-dependent manner. *J. Exp. Med.* **220**, e20220829 (2023). doi: [10.1084/jem.20220829](https://doi.org/10.1084/jem.20220829); pmid: [36346347](https://pubmed.ncbi.nlm.nih.gov/36346347/)
81. S. Chen *et al.*, SAMHD1 suppresses innate immune responses to viral infections and inflammatory stimuli by inhibiting the NF- κ B and interferon pathways. *Proc. Natl. Acad. Sci. U.S.A.* **115**, E3798–E3807 (2018). pmid: [29610295](https://pubmed.ncbi.nlm.nih.gov/29610295/)
82. J. Maelfait, A. Bridgeman, A. Benlahrech, C. Cursi, J. Rehwinkel, Restriction by SAMHD1 Limits cGAS/STING-Dependent Innate and Adaptive Immune Responses to HIV-1. *Cell Rep.* **16**, 1492–1501 (2016). doi: [10.1016/j.celrep.2016.07.002](https://doi.org/10.1016/j.celrep.2016.07.002); pmid: [27477283](https://pubmed.ncbi.nlm.nih.gov/27477283/)
83. J. Rehwinkel *et al.*, SAMHD1-dependent retroviral control and escape in mice. *EMBO J.* **32**, 2454–2462 (2013). doi: [10.1038/emboj.2013.163](https://doi.org/10.1038/emboj.2013.163); pmid: [23872947](https://pubmed.ncbi.nlm.nih.gov/23872947/)
84. J. R. Brestoff *et al.*, Intercellular Mitochondria Transfer to Macrophages Regulates White Adipose Tissue Homeostasis and Is Impaired in Obesity. *Cell Metab.* **33**, 270–282.e8 (2021). doi: [10.1016/j.cmet.2020.11.008](https://doi.org/10.1016/j.cmet.2020.11.008); pmid: [33278339](https://pubmed.ncbi.nlm.nih.gov/33278339/)
85. C. D. Camell *et al.*, Macrophage-specific de Novo Synthesis of Ceramide Is Dispensable for Inflammation-driven Inflammation and Insulin Resistance in Obesity. *J. Biol. Chem.* **290**, 29402–29413 (2015). doi: [10.1074/jbc.M115.680199](https://doi.org/10.1074/jbc.M115.680199); pmid: [26438821](https://pubmed.ncbi.nlm.nih.gov/26438821/)

86. H. Guo, J. P. Ting, Inflammasome Assays In Vitro and in Mouse Models. *Curr. Protoc. Immunol.* **131**, e107 (2020). doi: [10.1002/cpim.107](https://doi.org/10.1002/cpim.107); pmid: [33017103](https://pubmed.ncbi.nlm.nih.gov/33017103/)
87. J. Yan *et al.*, Tetramerization of SAMHD1 is required for biological activity and inhibition of HIV infection. *J. Biol. Chem.* **288**, 10406–10417 (2013). doi: [10.1074/jbc.M112.443796](https://doi.org/10.1074/jbc.M112.443796); pmid: [23426366](https://pubmed.ncbi.nlm.nih.gov/23426366/)
88. C. Jakobs, E. Bartok, A. Kubarenko, F. Bauernfeind, V. Hornung, Immunoblotting for active caspase-1. *Methods Mol. Biol.* **1040**, 103–115 (2013). doi: [10.1007/978-1-62703-523-1_9](https://doi.org/10.1007/978-1-62703-523-1_9); pmid: [23852600](https://pubmed.ncbi.nlm.nih.gov/23852600/)
89. R. Martí, B. Dorado, M. Hirano, Measurement of mitochondrial dNTP pools. *Methods Mol. Biol.* **837**, 135–148 (2012). doi: [10.1007/978-1-61779-504-6_9](https://doi.org/10.1007/978-1-61779-504-6_9); pmid: [22215545](https://pubmed.ncbi.nlm.nih.gov/22215545/)
90. P. M. Wilson *et al.*, A novel fluorescence-based assay for the rapid detection and quantification of cellular deoxyribonucleoside triphosphates. *Nucleic Acids Res.* **39**, e112 (2011). doi: [10.1093/nar/gkr350](https://doi.org/10.1093/nar/gkr350); pmid: [21576234](https://pubmed.ncbi.nlm.nih.gov/21576234/)
91. S. Bulst *et al.*, In vitro supplementation with deoxynucleoside monophosphates rescues mitochondrial DNA depletion. *Mol. Genet. Metab.* **107**, 95–103 (2012). doi: [10.1016/j.ymgme.2012.04.022](https://doi.org/10.1016/j.ymgme.2012.04.022); pmid: [22608879](https://pubmed.ncbi.nlm.nih.gov/22608879/)
92. S. Bulst *et al.*, In vitro supplementation with dAMP/dGMP leads to partial restoration of mtDNA levels in mitochondrial depletion syndromes. *Hum. Mol. Genet.* **18**, 1590–1599 (2009). doi: [10.1093/hmg/ddp074](https://doi.org/10.1093/hmg/ddp074); pmid: [19221117](https://pubmed.ncbi.nlm.nih.gov/19221117/)
93. Y. Sebti *et al.*, The LPS/D-Galactosamine-Induced Fulminant Hepatitis Model to Assess the Role of Ligand-Activated Nuclear Receptors on the NLRP3 Inflammasome Pathway In Vivo. *Methods Mol. Biol.* **1951**, 189–207 (2019). doi: [10.1007/978-1-4939-9130-3_15](https://doi.org/10.1007/978-1-4939-9130-3_15); pmid: [30825154](https://pubmed.ncbi.nlm.nih.gov/30825154/)
94. J. Y. Li *et al.*, The zebrafish NLRP3 inflammasome has functional roles in ASC-dependent interleukin-1 β maturation and gasdermin E-mediated pyroptosis. *J. Biol. Chem.* **295**, 1120–1141 (2020). doi: [10.1016/S0021-9258\(17\)49920-0](https://doi.org/10.1016/S0021-9258(17)49920-0); pmid: [31852739](https://pubmed.ncbi.nlm.nih.gov/31852739/)
95. J. J. Rahn, J. E. Bestman, K. D. Stackley, S. S. Chan, Zebrafish lacking functional DNA polymerase gamma survive to juvenile stage, despite rapid and sustained mitochondrial DNA depletion, altered energetics and growth. *Nucleic Acids Res.* **43**, 10338–10352 (2015). doi: [10.1093/nar/gkv1139](https://doi.org/10.1093/nar/gkv1139); pmid: [26519465](https://pubmed.ncbi.nlm.nih.gov/26519465/)
96. D. Liu *et al.*, Uncropped WB gels and HPLC data of article "Nucleotide metabolic rewiring enables NLRP3 inflammasome hyperactivation in obesity", Dryad (2026); <https://doi.org/10.5061/dryad.p2ngf1w47>.

ACKNOWLEDGMENTS

We thank UTSW Histopathology Core for their expertise in histological analysis. We also appreciate the UTSW Flow Cytometry Core for their technical support and the Metabolic Phenotyping Core [supported by a National Institutes of Health (NIH) grant P30DK127984] for assistance with body composition scanning and serum marker analysis. Additionally, we acknowledge UTSW Children's Research Institute Metabolomics Facility for their technical support with the Seahorse assay, the UTSW Quantitative Light Microscopy Core (QLMC) Facility for their assistance with the confocal microscopy, and the UTSW Metabolomics Core Facility for their expertise in HPLC-MS/MS detection of dNTPs. Figure S21 was created using BioRender.com. We are grateful to all members of the Zhong lab for their valuable discussions on this study. Lastly, we extend our thanks to S. Zhou, R. Wu, and C. Xing for their technical assistance. **Funding:** Z.Z. is a Cancer Prevention and Research Institute of Texas (CPRIT) Scholar and supported by a CPRIT New Investigator Recruitment Award (RR180014). This work was also funded by CPRIT Individual Investigator Research Awards (RP230261 to Z.Z. and RP200197 and RP240183 to S.L.), NIH grants (R35GM142654 and K22AI135074 to Z.Z., R01DK133283 to S.L., R01AI151708 to N.Y., R01AR075005 and R35GM136316 to E.H.C., and R35GM142689 to D.C.H.), and UT Southwestern Circle of Friends Awards (Z.Z.). **Author contributions:** Conceptualization: Z.Z., S.L.; Methodology: Z.Z., S.L., D.L., X.W., N.Y., J.R., D.C.H., E.H.C., H.B.; Investigation: D.L., C.Z., X.W., Z.L., R.X., S.H., L.G., X.L., S.Y., A.C., J.V., P.B., V.M.; Visualization: D.L., X.W., L.G., X.L.; Funding acquisition: Z.Z., S.L., N.Y., E.H.C., D.C.H.; Project administration: Z.Z., S.L.; Supervision: Z.Z., S.L.; Writing – original draft: D.L., S.L., Z.Z.; Writing – review & editing: D.L., S.L., Z.Z. **Competing interests:** The authors declare that they have no competing interests. **Data, code, and materials availability:** All data needed to evaluate the conclusions in the paper are present in the paper or the supplementary materials. The uncropped Western blot images and HPLC-MS/MS data are available in Dryad (96). **License information:** Copyright © 2026 the authors, some rights reserved; exclusive licensee American Association for the Advancement of Science. No claim to original US government works. <https://www.science.org/about/science-licenses-journal-article-reuse>

SUPPLEMENTARY MATERIALS

science.org/doi/10.1126/science.adq9006

Figs. S1 to S21; Data S1 and S2

Submitted 5 June 2024; resubmitted 18 February 2025; accepted 30 September 2025

10.1126/science.adq9006